Stony Brook University

A Comprehensive Investigation and Coupler Design for Higher-Order Modes in the BNL Energy Recovery Linear Accelerator

A Thesis Presented

by

Carlos Marques

to

The Graduate School

in Partial Fulfillment of the Requirements

for the Degree of

Master of Science

in

Physics

(Scientific Instrumentation)

Stony Brook University

May 2014

Stony Brook University

The Graduate School

Carlos Marques

We, the thesis committee for the above candidate for the Master of Science degree, hereby recommend acceptance of this thesis.

Sergey Belomestnykh - Thesis Advisor
Adjunct Professor, Department of Physics and Astronomy
Stony Brook University

Xu Du
Assistant Professor, Department of Physics and Astronomy
Stony Brook University

Thomas Hemmick
Distinguished Teaching Professor, Department of Physics and Astronomy
Stony Brook University

Dmitri Tsybychev
Assistant Professor, Department of Physics and Astronomy
Stony Brook University

This thesis is accepted by the Graduate School.

Charles S. Taber
Dean of the Graduate School

Abstract of the Thesis

A Comprehensive Investigation and Coupler Design for Higher-Order Modes in the BNL Energy Recovery Linear Accelerator

by

Carlos Marques

Master of Science

in

Physics

(Scientific Instrumentation)

Stony Brook University

2014

A next generation Energy Recovery Linac (ERL) is under development in the Collider-Accelerator Department at Brookhaven National Laboratory (BNL). This ERL uses a superconducting radio frequency (SFR) cavity to produce an electric field gradient ideal to accelerate charged particles. As with many accelerators, higher-order modes (HOMs) can be induced by a beam of charged particles traversing the linear accelerator cavity. The excitation of these modes can result in problematic single and multi-bunch effects and also produce undesirable heat loads to the cryogenic system. Understanding HOM prevalence and structure inside the accelerator cavity is crucial for devising a procedure for extracting HOM power and promoting excellent beam quality. In this work, a method was created to identify and characterize HOMs using a perturbation technique on a copper (Cu) cavity prototype of the BNL3 linac and a double $\lambda/4$ crab cavity. Both analyses and correlation between simulated and measured results are shown. A coaxial to dual-ridge waveguide HOM coupler was designed, constructed and implemented to extract power from HOMs simultaneously making an evanescent fundamental mode for the BNL3 cavity. A full description of the design is given along with a simulated analysis of its performance. Comparison between previous HOM coupler designs as well as correspondence between simulation and measurement is also given.

Dedicado aos meus queridos avós.

Contents

List of Figures

List of Tables

Abbreviations

RHIC	**R**elativistic **H**eavy **I**on **C**ollider
ERL	**E**nergy **R**ecovery **L**inac
BNL	**B**rookhaven **N**ational **L**aboratory
HOM	**H**igher **O**rder **M**ode
QCD	**Q**unatum **C**hromo**D**yanmics
SRF	**S**uperconducting **R**adio **F**requency
EM	**E**lectro**M**agnetic
TE	**T**ransverse **E**lectric
TM	**T**ransverse **M**agnetic
BBU	**B**eam **B**reak-**U**p
MWS	**M**icro**W**ave **S**tudio
CAD	**C**omputer **A**ided **D**esign
TEM	**T**ransverse **E**lectro-**M**agnetic
WG	**W**ave**G**uide
DR	**D**ual-**R**idge
IC	**I**nter**C**onnect
HL-LHC	**H**igh **L**uminosity - **L**arge **H**adron **C**ollider
CC	**C**rab **C**avity
EDM	**E**lectric **D**ischarge **M**achining

Acknowledgements

First and foremost, I would like to thank my advisor Sergey Belomestnykh for introducing me to this new line of research. His patient guidance, attention to detail and confidence in my ability has allowed me to grow as a professional. Without his extensive understanding and knowledge of superconducting RF science and accelerator physics, generosity and strong leadership, this work would simply not have been possible. It has been a great honor and privilege to study under his guidance.

I wish to thank Harald Hahn for our creative exchanges and for challenging me with worthwhile problems and curiosities. Harald was a vital contributor to the higher order mode characterization measurements and analysis. A special thanks to Robert Kellermann and Tom Seda who were always willing to help me overcome technical challenges and for enduring my jokes. I would like to also thank Wencan Xu, Ilan Ben-Zvi, Binping Xiao, Qiong Wu, Karim Hamdi, Scott Seberg and Silvia Verdu Andres for our helpful discussions and your contributions to this thesis.

Last but not least, I would like to thank my friends and family who have always supported me throughout. They are my inspiration and give me the courage and commitment to overcome the trials of life.

Chapter 1

Introduction

We begin with a brief overview of an effort to revamp the Relativistic Heavy Ion Collider (RHIC) as an electron-ion collider, a project known as eRHIC. Followed by a brief description of an energy recovery linac (ERL) at Brookhaven National Laboratory (BNL) which has a vital role in the realization of a linac-ring eRHIC experiment. Finally higher order modes (HOMs) are discussed; their physical origin, role in accelerator cavities and their significance associated with this thesis.

1.1 The eRHIC Project

The Standard Model is a paradigm for theoretical particle Physics concerning the fundamental interactions, namely the strong, weak and electromagnetic. It is a prized theory leading to several successful predictions and Nobel Prizes in Physics. In fact, the most recent Noble Prize in Physics to date was awarded to Peter Higgs and François Englert for their theoretical discovery of a mechanism that contributes to our understanding of the origin of mass of subatomic particles, which was experimentally confirmed at the Large Hadron Collider. This extremely scientifically significant mechanism known as the Higgs mechanism, is a milestone for the Standard Model.

The Standard Model component for the strong force is called Quantum Chromodynamics (QCD) which describes the interactions between quarks and gluons. Various experiments have quantitatively verified QCD, the 1990 and 2004 Noble Prizes in Physics were both awarded for work on QCD, but many questions remain. The eRHIC proposal was set forth to unveil some of the mysteries behind QCD by either precision measurements or discovering novel physics which will expose underpinnings in the theory. The goal for this project is to upgrade the existing RHIC facilities as an ion-ion collider

to an electron-ion collider with the appropriate specifications to probe the interactions between quarks and gluons; a project that has culminated from decades of experiments from CERN, DESY, Fermilab, and SLAC accelerator facilities as well as simulations performed across the scientific community. By testing QCD, we take a step closer to understanding the fundamental structure of matter and 99% of the observable mass in the physical universe [1, 2]. A proposed schematic of a linac-ring design can be seen in Fig. 1.1.

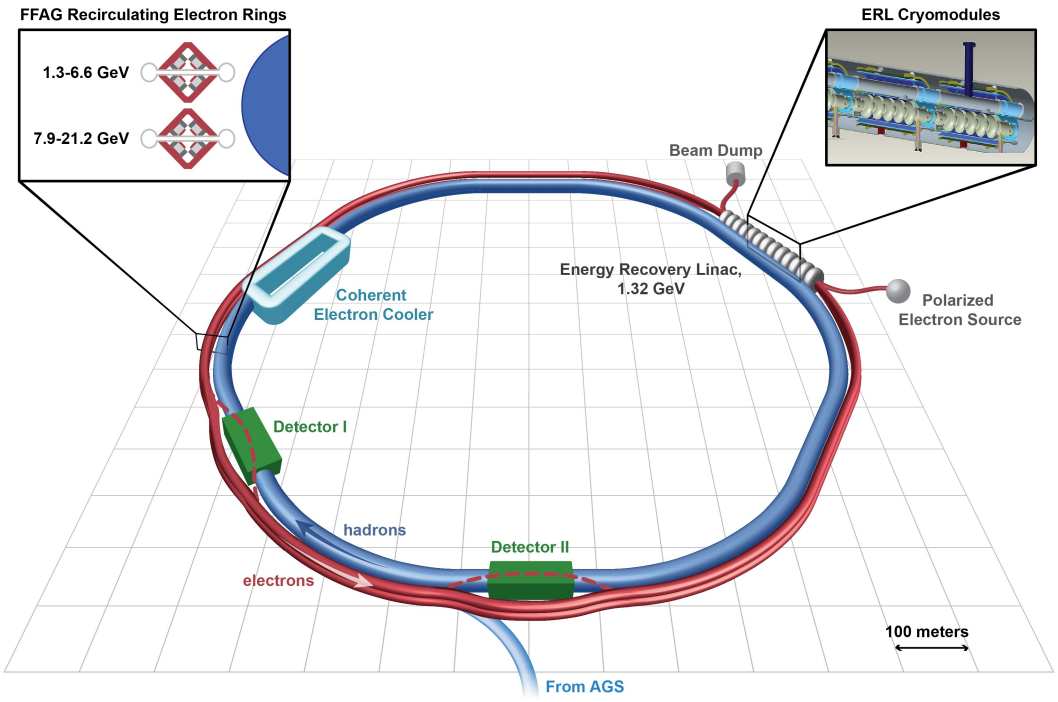

FIGURE 1.1: A schematic layout of a possible linac-ring eRHIC design.

1.2 The ERL at BNL

Among many of the proposed upgrades for eRHIC, a linac-ring design is under consideration. This upgrade consists of using an ERL to accelerate a polarized electron beam to collide with the polarized RHIC beam [1, 3]. The most basic ERL is a linear accelerator (linac) which produces accelerated bunches that are looped back into the low-energy side of the linac π out of phase from the accelerating mode. The revisiting bunches are then decelerated and dumped, efficiently depositing their energy into the cavity fields, which are then used to accelerate subsequent bunches [4]. The R&D ERL at BNL is a proof of principle effort designed for testing concepts for high-energy coherent electron cooling and electron-ion colliders, both are essential for the linac-ring consideration. The

ERL is composed of a superconducting radio frequency (SRF) photocathode half cell gun, a 5-cell SRF cavity and achromatic flexible optics. The operating frequency of the accelerating mode for this design is set to 703.75 MHz which is the 25^{th} harmonic of the RHIC with 360 bunches. A schematic of the BNL R&D ERL can be seen in Fig. 1.2 [5].

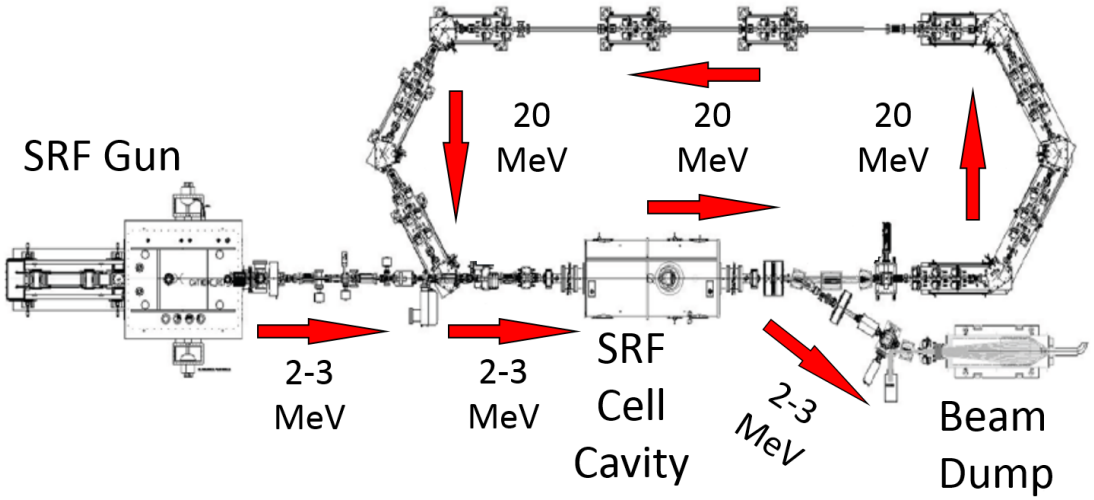

FIGURE 1.2: A schematic layout of the BNL R&D ERL.

Currently most of the R&D ERL subsystems are designed, built, tested and many even installed. With commissioning underway, the need to resolve technical issues associated with the final design is crucial.

1.2.1 SRF Cavity

At the heart of the ERL is a SRF 5-cell niobium cavity known as BNL3. This cavity is responsible to supply energy, specifically kinetic energy, to the charged particles via a longitudinal electric field. Assuming that the charged particle is in phase with the RF signal in the cavity, the particle will accelerate with a voltage gain

$$V_c = \left| \int_0^d E_z e^{i\omega_0 z/c} dz \right|$$

where E_z is the longitudinal electric field, d is the cavity length and ω_0 is the fundamental (angular) frequency or simply the mode. The time averaged energy of the electric field equals that of the magnetic field, therefore the total energy in the cavity is given by

$$U = \frac{\mu_0}{2} \int_V |\mathbf{H}|^2 dv = \frac{\epsilon_0}{2} \int_V |\mathbf{E}|^2 dv$$

where the integral is over the total volume of the cavity and where μ_0 and ϵ_0 are the permeability and permittivity of free space respectfully. Furthermore the power dissipated

in the cavity walls associated with Joules heating can be calculated as

$$P_c = \frac{R_s}{2} \int_S |\mathbf{H}|^2 ds$$

where R_s is the surface resistance of the cavity walls and the integral is over the cavity surface. The above equations lead to an important figure of merit known as the quality factor

$$Q_0 = \frac{\omega_0 U}{P_c}$$

where Q_0 is 2π times the energy stored over the energy dissipated per cycle or in other words 2π times the number of cycles it takes to dissipate the energy stored in the cavity. This result also demonstrates the motivation for using a superconducting cavity where R_s is reduced to the residual resistance, typically on the order of tens of nano-Ohms in the superconducting state, yielding $Q_0 \approx 10^{10}$ [6, 7]. The quality factor for the SRF 5-cell niobium cavity has a simulated value of $Q_0 = 2 \times 10^{10}$[8].

1.3 Higher Order Modes

Accelerator cavities operate as a transmission system between the RF power source to the charge bunch via a longitudinal electric field. Conversely, accelerated bunches passing through the cavity deposit electromagnetic (EM) wakefields which could excite modes inside the cavity. These excited modes are generally above the fundamental mode and are known as HOMs. Every mode is defined by the cavity geometry. Therefore by solving Maxwell's equations for EM radiation using the appropriate boundary conditions, we obtain the eigenvalues or eigenmodes associated with that particular geometry. In the case where the system or cavity is nonintegrable, we rely on numerical methods and/or statistics to approximate the eigenmodes[9]. In either case, we can determine or approximate the EM field distributions as well as the propagation constants for any particular cavity.

Two characteristic modes are commonly used to identify resonances in an accelerator cavity namely transverse electric/magnetic (TE/TM) modes. Each mode is an orthogonal set established from the solution of Maxwell's equations on the transverse field components with Dirichlet and Neumann boundary conditions or

$$E_z|_S = 0 \quad \text{and} \quad \left.\frac{\partial H_z}{\partial n}\right|_S = 0$$

respectfully. E_z and H_z are the longitudinal electric and magnetic fields respectfully and n is the unit normal vector with respect to the cavity surface S. These modes

are typically denoted TE_{mnp} and TM_{mnp} where the indexes m, n and p are integers which represent sign changes or number of nodes in the three dimensional orthogonal coordinate system. We focused our discussion to only TM and TE modes since all other modes, such as Transverse Electro-Magnetic (TEM) ($E_z = H_z = 0$) or hybrid modes ($E_z \neq 0, H_z \neq 0$), may be expressed as a superposition of these. Additionally, TE modes do not have a longitudinal electric field component and therefore cannot be used to accelerate charged particles. To further help identify different types of modes and field distributions, both detrimental and beneficial to the accelerator cavity, the expressions monopole, dipole and quadrupole are commonly used. TM_{0np} type field distributions are referred to as monopole modes, TM_{1np} as dipole modes, TM_{2np} as quadrupole modes, etc. For example, let us consider a cylindrical coordinate system, the fundamental mode would normally be represented as the first monopole mode for its lowest frequency TM_{010} and the values of m, n and p represent sign changes in the ϕ, ρ and z directions respectively. This sign change in the ρ direction creates a magnetic field vortex centered around the $\hat{z}$ direction inducing an ideal field for accelerating charged particles i.e. maximum and unvarying electric field on the z axis. Examples of monopole, dipole and quadrupole modes can be seen in Figure 1.3.

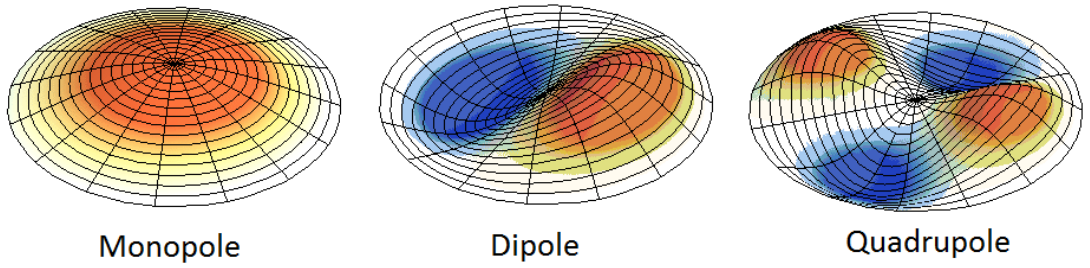

FIGURE 1.3: Artist's rendition of HOMs. White shading represents regions near zero amplitude of the electric field.

1.3.1 HOM Consequences in Accelerator Cavities

As mentioned in the previous section, an ideal accelerating cavity produces a uniform electric field in the direction of beam propagation at the operating/fundamental mode. Any other modes serve no purpose except to produce on and off axis fields that are detrimental to the beam quality. Dipole modes are especially harmful to beam quality and introduce transverse instabilities because of their strong near axis deflecting electric field. Additionally, charge bunches interacting with high order monopole modes create a harmful energy spread known as longitudinal instabilities. If these HOMs are not suppressed they could lead to beam instabilities and in some cases results in complete beam loss, a scenario known as Beam Break-Up (BBU). In superconducting cavities, HOMs

also produce additional cryogenic losses from power dissipation on the cavity walls, resulting in additional expenses towards refrigerants. Typically the cavity cell count and geometric parameters are optimized to avoid trapped HOMs and reduce the longitudinal and transverse wakefields as much as possible. As the name suggests, a trapped mode is a mode which is confined to local discontinuities and in this case trapped modes are confined in the active cells of the BNL3 cavity. Consequently trapped modes do not propagate through the beam end tubes and could potentially remain unperturbed inside the linear accelerator. However, these parameters influence the degradation of the fundamental mode and ultimately the accelerator performance. Therefore to alleviate these problems and optimize accelerator performance, sufficient HOM damping is required while retaining the fundamental mode.

HOM damping requirements are specified by the beam characteristics. The average monopole HOM power is given by the equation

$$P_{\text{ave}} = k_{||} Q_B I_B$$

where $k_{||}$ is the cavity loss factor which is described in more detail below, Q_B is the bunch charge and I_B beam current. The beam current is calculated by

$$I_B = n Q_B F_B.$$

where n is the number of passes and F_B is the bunch frequency. Using the eRHIC parameters of a calculated cavity loss factor of 3.6 V/pC for a 2 mm Gaussian bunch length, bunch charge of 3.5 nC, beam current of 50 mA, combined 12 passes (6 accelerating and decelerating) and bunch frequency of 9.4 MHz yields a monopole HOM average power approximately 7.5 kW per cavity[10]. Removing this power presents a formidable task and is one of the motivations for this thesis as well as other work [11].

The average energy lost by a charge to a dipole mode is

$$U_q = k_d q^2 \left(\frac{\rho}{a}\right)^2$$

where q is the charge of the particle, ρ is the distance off axis, a is the beam tube radius and k_d is the dipole loss factor given by

$$k_d = a^2 \left(\frac{\omega_m}{c}\right)^2 \frac{\omega_m}{4} \frac{R_d}{Q_d}.$$

ω_m is the eigenfrequency of the mode, Q_d is the quality factor for the dipole mode and R_d is the dipole shunt impedance. Observe that the ratio of R_d/Q_d, commonly referred to as "R over Q", is proportional to the dipole loss factor and is the only unknown. This

loss factor can be generalized to excitations or wakefield amplitudes from any mode and can be represented as R_m/Q_m where R_m and Q_m is the shunt impedence and quality factor of the m^{th} mode respectfully. R_m determines the level of mode excitation by charges passing through the cavity of the m^{th} mode which is not to be confused with the index m representing nodes on an orthogonal coordinate system for the TE/TM modes. For excellent accelerator performance, suppression of R_m/Q_m for detrimental HOMs is key.

1.3.2 HOM Simulations

We have briefly discussed the fundamental mode for a cylindrical coordinate system and how it is ideal for accelerating charged particles in Section 1.3. Similar analysis is made for accelerator cavities with a more sophisticated geometry like that of the BNL3 cavity and its predecessors the BNLI and BNLII cavities [8, 12]. A copper (Cu) BNL3 cavity can be seen in Figure 1.4. The BNL3 cavity is the newest prototype optimized for the eRHIC project. A Cu analog of the BNL3 cavity is used to perform measurements and acquire insight into technical challenges before finalizing a niobium SRF Cavity. The geometry of this cavity was designed to achieve various accelerator parameters at 703.75 MHz, discussed in detail elsewhere[10]. Analytic solutions can only be achieved for the most trivial configurations and therefore we generally use numerical methods to approximate the mode frequencies and EM fields. One of the programs available from the Collider-Accelerator Department at BNL to solve for EM fields and modes associated with any geometry is called CST Microwave Studios ®(MWS). This program uses a 3D computer aided design (CAD) front end to construct any abstract cavity and its components. Once the CAD is rendered, MWS has various solvers including transient, frequency domain, eigenmode to compute cavity modes, EM fields, frequency dependencies, etc [13]. We can also solve for various ratios like R/Q, $E_{\text{peak}}/\sqrt{U}$, $E_{\text{peak}}/E_{\text{acc}}$, $H_{\text{peak}}/\sqrt{U}$, etc. The simulated HOM field distributions and eigenfrequencies are then used as a comparison with measurements and HOM characterizations which will be discussed in greater detail in Chapter 2.

1.3.3 HOM Measurements

The correlation between the simulated versus measured HOMs, can be found using various techniques. The technique used in this thesis was by evaluating scattering parameters or S-parameters, specifically S_{21} on the BNL3 Cu cavity by using an Agilent E5071C ENA network analyzer[14]. S_{21} for the network analyzer as well as the CST

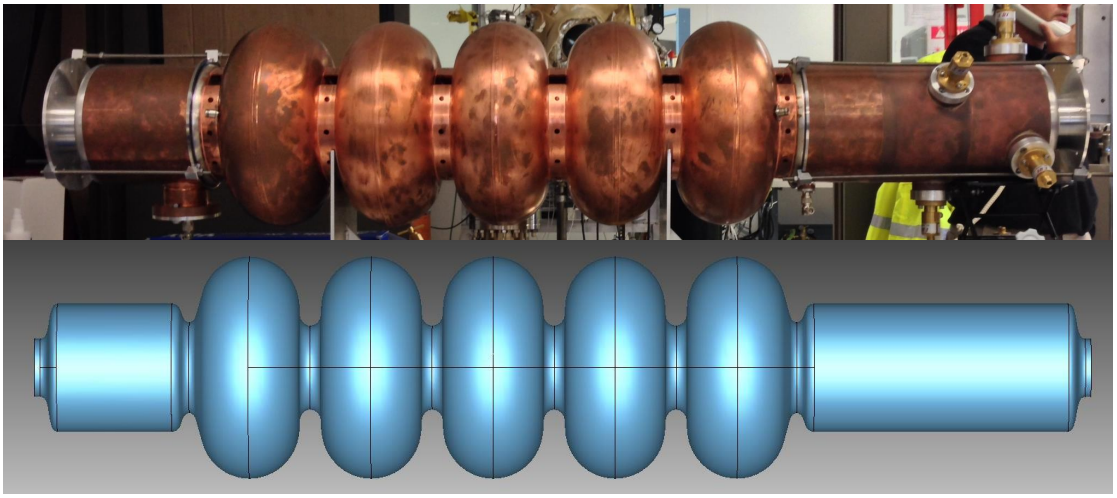

FIGURE 1.4: The top photograph is of the BNL3 R&D Cu cavity while the bottom is a Microwave Studio 3D CAD representation of the BNL3 Cavity. The cavity cells are enumerated in sequential order from left to right, where cell 1 is the leftmost cell.

MWS software is defined as

$$S_{21}(dB) = 20\log_{10}\left(\frac{V_{\text{out}}}{V_{\text{in}}}\right)$$

where V_{in} and V_{out} is the incident and outgoing voltage respectfully. Voltage is not to be confused with field intensity which is proportional to the square of the voltage, hence the factor of 2. Eigenmodes are easily identifiable by spikes in the S_{21} measurement versus frequency which can then be compared to simulated results. Analyzing the peaks also yields the quality factor for any observable mode by

$$Q = \frac{f_0}{\Delta f}$$

where f_0 is the eigenfrequency and Δf is the full width at -3dB from maximum peak height. Data from the network analyzer can be found in Figure 1.5. S_{21} measurements are influenced by the position of the incident and outgoing power from the network analyzer. In other words, if either network analyzer port is located on a node of a mode then the mode will not be excited or measured. To avoid absent modes, measurements are made at different positions of the cavity and then these data are combined for a full mode spectrum. More detail about HOM measurements can be found in Chapter 2.

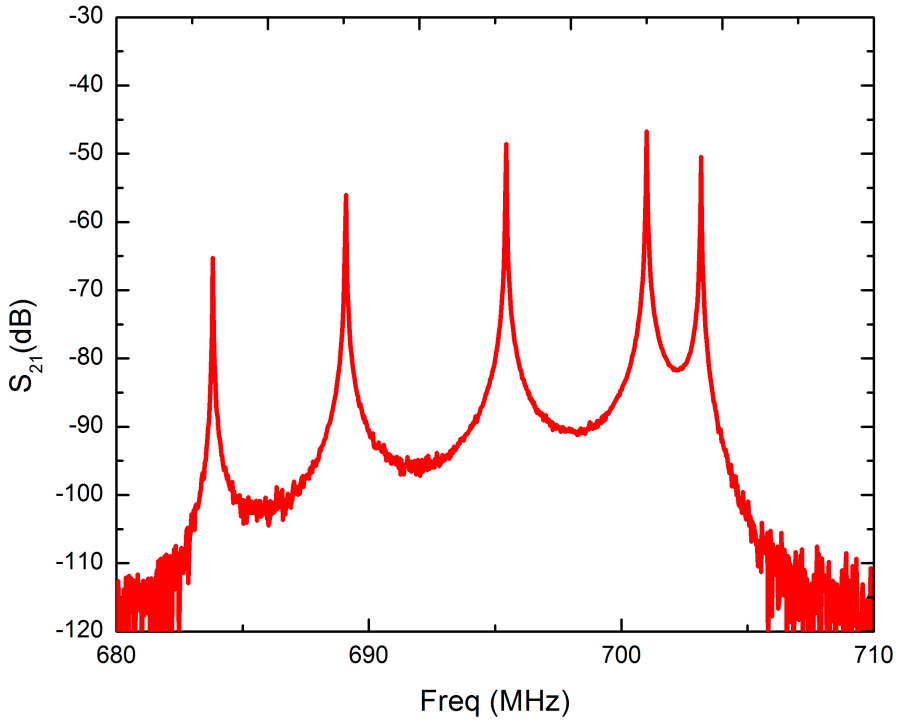

FIGURE 1.5: Example data taken from the fundamental passband of the BNL3 Cu cavity using the Agilent E5071C ENA network analyzer. The middle peak has a corresponding $Q \approx 34000$.

1.3.4 HOM Couplers

The basic principle behind HOM couplers is to allow unwanted HOM power to propagate out of the cavity and into an RF load while simultaneously preserving power for the fundamental mode. In this section, three major types of couplers (AKA dampers) are discussed namely waveguide (WG), coaxial and ferrite load couplers. In Chapter 4, a coaxial to WG coupler designed for transferring HOM power from the BNL3 cavity to an RF load will also be discussed.

Ferrite HOM absorbers are usually composed of a sintered material with the permeability and permittivity consistent with zero-specular-reflection in the rf spectrum. The microwave absorbing characteristics are controlled by the choice of materials, material composition and manufacturing procedures but are typically designed to have a broadband absorption spectrum. A HOM absorber would be constructed by lining the cavity end tube walls with ferrite absorbers; a relatively simple construction. Since the lining is covering all surfaces of the beam tube then these HOM absorbers would reduce all HOM power, including any induced polarizations of HOMs. They would also be

operating outside the cryostat and water cooled since they quickly heat up due to the power absorption. However, these absorbers also absorbs power from the fundamental mode. Since end tubes serve as a natural filter for the fundamental mode as well as a high power conduit, this lining must be sufficiently far away from the active cells so that fundamental mode power is not absorbed. This leads to a reduction of one of the most decisive characteristics of a superconducting linear accelerator the real-estate gradient

$$E^*_{\text{acc}} = \frac{dE/e}{l_{\text{cav-cav}}}$$

where dE is the energy gained after a full pass through the accelerator, e is the electron charge and $l_{\text{cav-cav}}$ is the cavity to cavity length. This is not to be confused with the real-estate gradient for a accelerator cavity

$$E_{\text{acc}} = \frac{dE/e}{l_{\text{cell-cell}}}$$

where $l_{\text{cell-cell}}$ is the cell to cell distance and is defined as $\beta\lambda/2$ where $\beta = v/c$ or the ratio of the particle velocity over the speed of light. Originally the R&D ERL was designed to support ferrite HOM absorbers however because of these setbacks other HOM schemes are being actively investigated. The BNL1 assembly with ferrite dampers as well as a prototype HOM ferrite damper can be seen in Figure 1.6[15].

Among the simplest couplers conceptually is a hollow metallic rectangular WG which can propagate TM and TE modes but cannot propagate TEM modes since the metallic walls serve as only one conductor. This WG is among the easiest to construct and the field distributions are trivial to solve analytically. The dimensions of the rectangular WG are determined by the cut-off frequency and sufficient power transmission. The lowest order mode able to propagate inside the rectangular WG is $\lambda/2$, where $\lambda/2$ is precisely the length of the longest leg of the cross section dimension of the rectangular WG and should be selected to accommodate the lowest frequency HOM. Modes of larger wavelength/lower frequency ($\lambda = c/f$) will be attenuated, so called evanescent waves and as a result WGs offer a natural solution as a HOM coupler. This RF equivalent of a high pass filter eliminates the need to place the HOM coupler far away from the active cells which leads to an increased real-estate gradient compared to the ferrite damper. An example cavity using waveguide HOM couplers can be seen in Figure 1.7.

A cross-sectional representation of the fundamental mode field distribution of a rectangular WG can be seen in Figure 1.8. The overall power transfer is defined by the cross sectional area or

$$P_T = \int_A P_z dA \quad \text{and} \quad P_z = \text{Re}(\mathbf{E} \times \mathbf{H}^*) \cdot \hat{z}$$

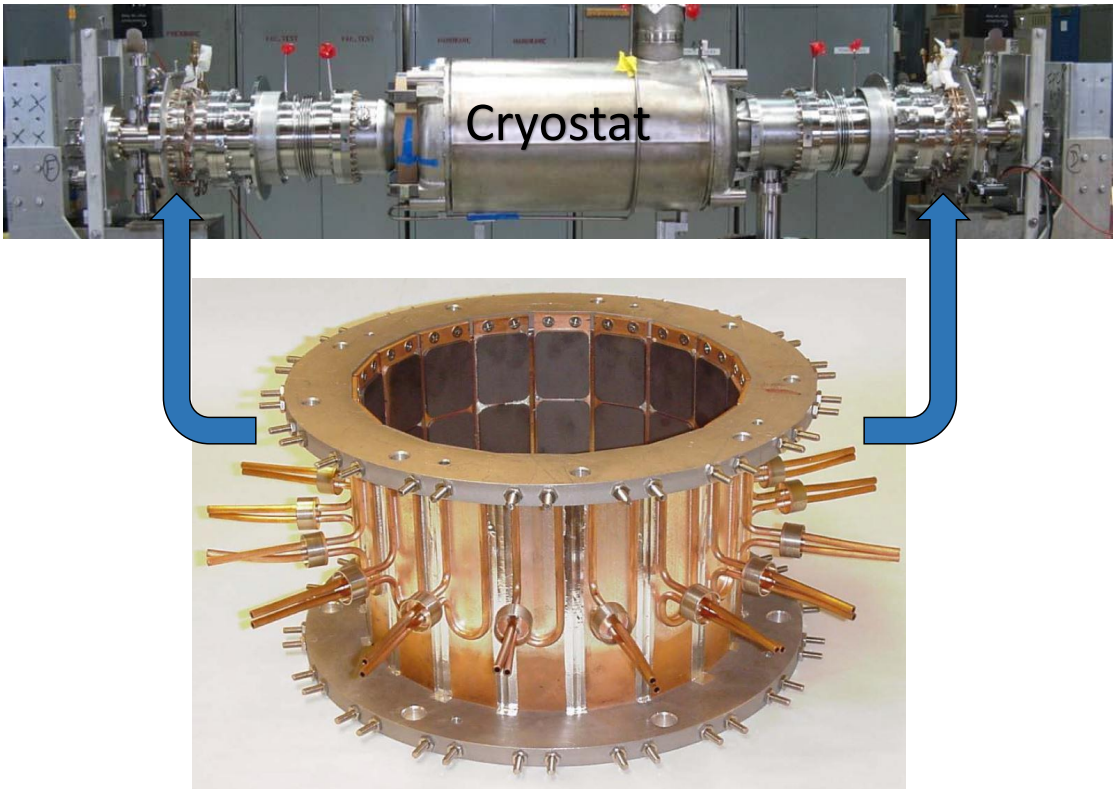

FIGURE 1.6: The top is a photograph of the BNL1 assembly where the accelerator cavity is located in the helium filled cryostat. The bottom is a photograph of a prototype HOM ferrite damper and the arrows point to the physical location of absorbers on the assembly.

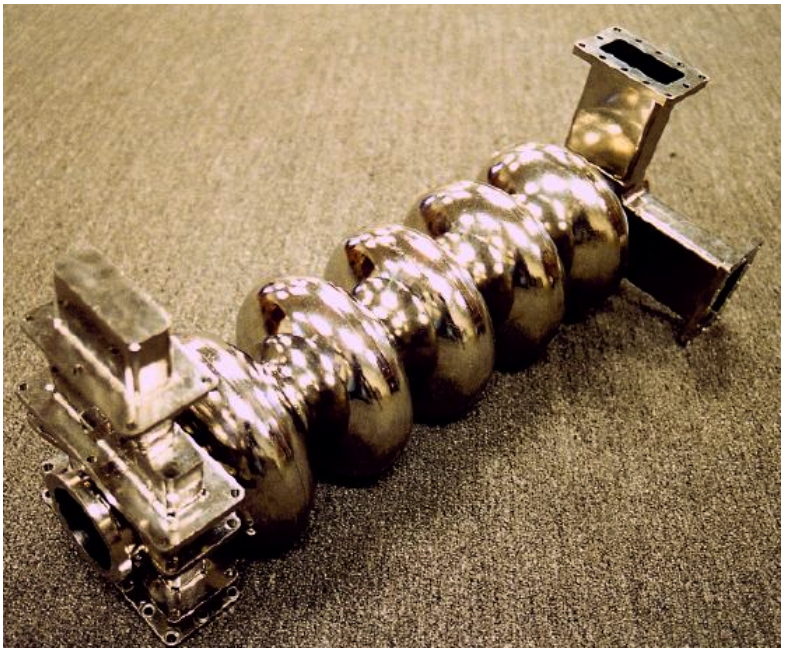

FIGURE 1.7: CEBAF five cell linear accelerator cavity using WG HOM couplers courtesy of Cornell-LEPP.

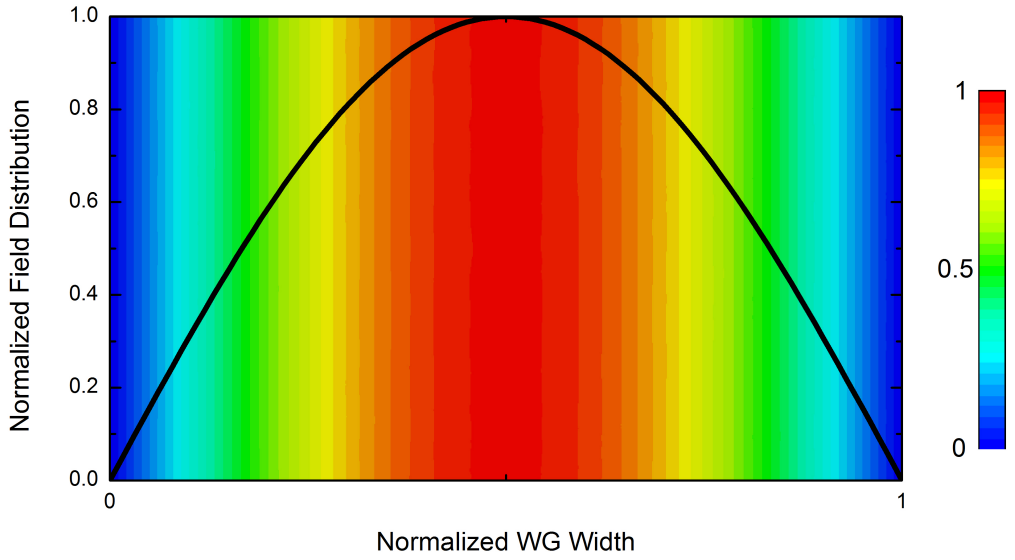

FIGURE 1.8: Cross-section representation of the TE_{010} electric field distribution of a rectangular waveguide.

where P_z is z component of the Poynting vector, A is the cross sectional area and P_T is the power transmitted. Hence, WGs offer a means of large power extraction if their cross sectional area is relatively large compared to the operating wavelength.

The major disadvantage when working with rectangular WGs is their relatively large size, in turn leading to a large cryostat to accommodate the WGs. For example, to ensure proper attenuation so that the fundamental mode does not reach the RF terminating load, the length of the WG must be long compared to the fundamental wavelength. Additionally, operating in the RF spectrum consequently leads to a large WG cross sectional area. For example, using 825MHz $\lambda/2 \approx 17.6$cm which is considerably large compared to the beam tube of the BNL3 Cavity (21cm). This is especially important when damping all HOM polarizations by using multiple WGs arranged around the beam tube.

Coaxial couplers are typically compact and comprise an inner and outer conductor to extract HOM power. With the inner conductor, coaxial couplers are capable of propagating TEM, TE, TM and even hybrid modes and are ideal for lower frequencies since even DC power is transferable. In order to reject the fundamental mode from propagating to the RF load through the coaxial coupler, a parallel LC circuit, effectively a high pass filter, is added in series between the RF load and the cavity. The RF

equivalent for inductance and capacitance respectfully is

$$L = \frac{\mu}{|I_0|^2}\int_S \mathbf{H}\cdot\mathbf{H}^* ds \quad , \quad C = \frac{\epsilon}{|V_0|^2}\int_S \mathbf{E}\cdot\mathbf{E}^* ds$$

where $\mu = \mu_r\mu_0$ and $\epsilon = \epsilon_r\epsilon_0$ is the permeability and permittivity of the material filling the coaxial filter respectfully, I_0 and V_0 is the current and the voltage in the line respectfully and S is the cross sectional surface area between the inner and outer conductor of the coaxial line. The distinction between circuit theory and transmission line theory is discussed extensively [6, 7, 16]. Similarly to WG couplers, coaxial couplers are placed in relatively close proximity to the active cells allowing a larger real-estate gradient compared to the ferrite load dampers. A prototype coaxial coupler was designed for the extraction of HOMs in the BNL3 cavity and a schematic of this coupler can be seen in Figure 1.9. The coupling probe on the end of the coupler is responsible to capacitively (or inductively) couple to the local field inside the beam tube. As a result, the BNL3 cavity will support three coax couplers on each side of the active cavities, with an azimuthal separation of 120°, to extract the HOM polarizations. A plot of the S_{21} performance of the coaxial HOM coupler can be found in Figure 1.10[17].

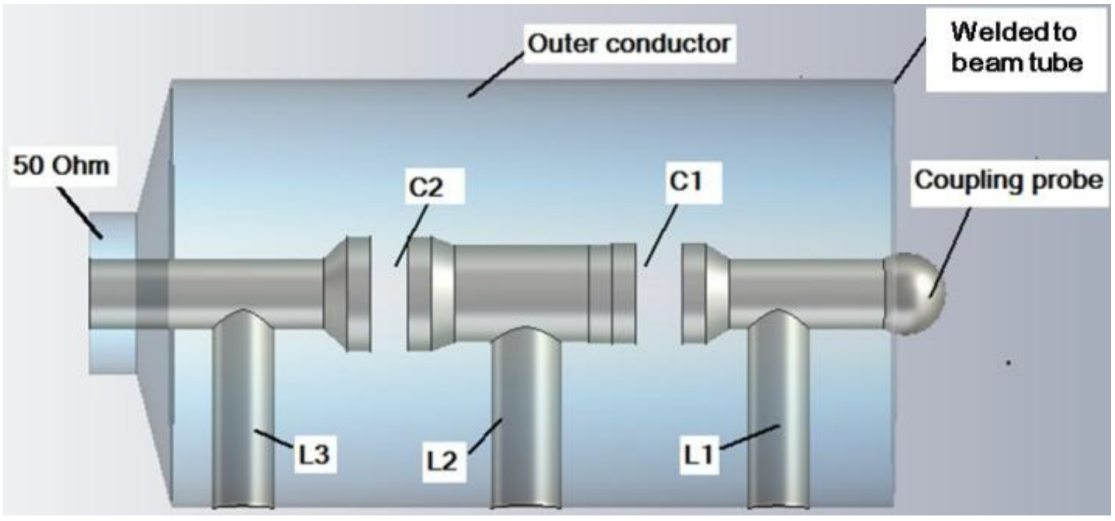

FIGURE 1.9: Schematic of the 2-stage HOM coupler by W. Xu.

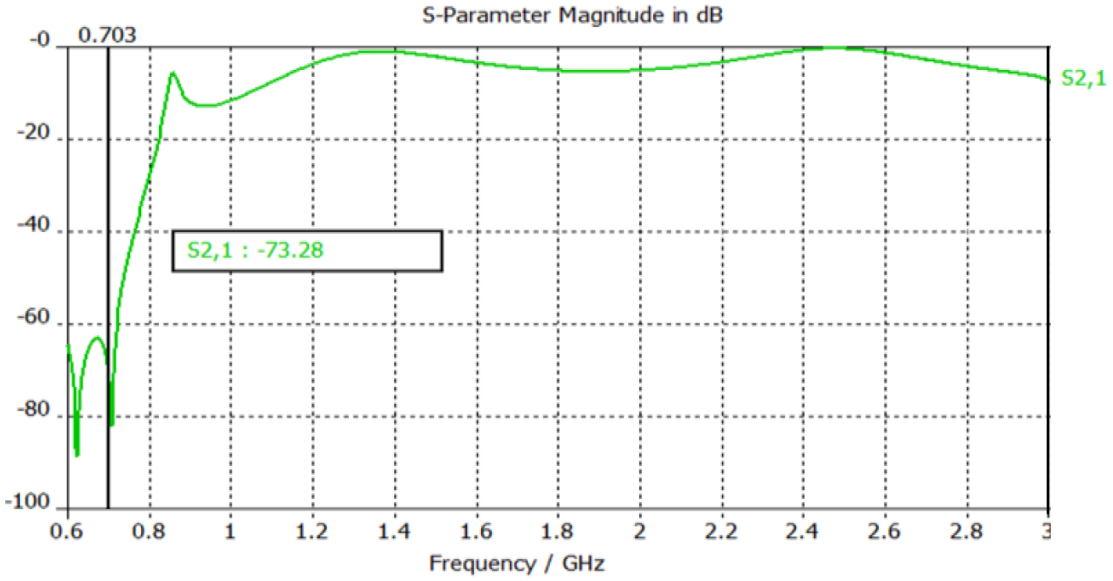

FIGURE 1.10: S_{21} of the Coaxial HOM coupler shown above.

Chapter 2

HOM Measurements

The following chapter describes the methods used to fully characterize HOMs in the BNL3 Cu cavity. Correspondence between measurement and simulation are also given and the importance of their agreement is discussed.

2.1 The Bead Pulling Technique

Also known as the Slater method, the bead pulling technique is a measurement technique which uses a relatively small dielectric or conductive perturbation (in this case a dielectric cylinder) that runs through an open cavity while simultaneously measuring the phase (and/or amplitude) of the field at a fixed frequency. The bead is small relative to the driving frequency and the coupling to the local field surrounding the bead depends on the material properties of the bead. For example, while a metallic bead is susceptible to both electric and magnetic fields, a dielectric bead will be susceptible exclusively to electric fields. Geometric factors of the bead also play a role in the total perturbation of the local fields. A needle-like conductor will be sensitive to longitudinal electric fields while relatively invisible to transverse magnetic fields, ideal for measuring TM modes. The expression below gives the relative frequency shift corresponding to this perturbation method,

$$\frac{\Delta\omega}{\omega_0} = F_H \frac{\mu_0 \mathbf{H}' \cdot \mathbf{H}'^*}{U} - F_E \frac{\epsilon_0 \mathbf{E}' \cdot \mathbf{E}'^*}{U}.$$

$\Delta\omega = \omega - \omega_0$, F_H and F_E are relative geometric factors which quantify the local coupling of the perturbed magnetic $\mathbf{H}'$ and electric $\mathbf{E}'$ fields respectively and a table of perturbation factors can be found in Table 2.1. U is the total stored energy inside the cavity as defined above[12]. This technique is widely used in the accelerator

Bead	F_E	F_H
Metallic Sphere	πr^3	$\frac{\pi r^3}{2}$
Metallic cylinder, $\|\|$ field, $l/r >> 1$	$\frac{\pi}{24}\frac{l^3}{\ln(l/r)-1}$	$\frac{\pi}{6}lr^2$
Metallic cylinder, $\perp$ field, $l/r >> 1$	$\frac{\pi}{3}lr^2$	$\frac{\pi}{3}lr^2$
Dielectric Sphere	$\pi r^3\frac{\epsilon-1}{\epsilon+2}$	-
Dielectric cylinder, $\|\|$ field, $l/r >> 1$	$\frac{\pi}{24}\frac{(\epsilon-1)l^3}{(\epsilon-1)\left(\ln\frac{l}{r}-1\right)-\left(\frac{(l)}{(2r)}\right)^2-\frac{3}{2}}$	-
Dielectric cylinder, $\perp$ field, $l/r >> 1$	$\frac{\pi}{12}\frac{(\epsilon-1)l^3}{(\epsilon-1)\left(\ln\frac{l}{r}-1\right)-\frac{(\epsilon-1)}{(\epsilon+1)}\left(\left(\frac{l}{2r}\right)^2-\frac{3}{2}\right)}$	-

TABLE 2.1: Geometric field perturbation factors, where r, l are the radius and length of the bead respectfully.

community[6, 11, 12, 18, 19] and a schematic of our bead pulling assembly can be found in Figure 2.1.

The bead pulling assembly is mounted on four manual linear translational stages. These stages constrain movement in the x and y plane and help precisely align the bead for on and off-axis measurements. The bead is glued to fishing line and the line is tensioned around pulleys that are mounted on the stages, through the open cavity and finally tied together. A moveable anchor is placed on the suspended fishing line and acts as a tensioner. The cavity is fixed throughout the experiment and should be isolated from sudden temperature changes and vibrations. A computer driven stepper motor is used to precisely move the bead longitudinally through the cavity. For this specific measurement, an Agilent E5071C ENA network analyzer was used to supply input power to port 1 and measure transmission S_{21} from port 2 at a fixed frequency. The frequency is fixed on an eigenmode and the relative phase is measured throughout the cavity. Although the network analyzer measures both amplitude and phase, the phase is more susceptible to the change in frequency if the initial frequency is an eigenmode and can be translated with the relation

$$S_{21} = |S_{21}|e^{i\Phi} = \frac{2Q_L}{\sqrt{Q_{\text{in}}Q_{\text{out}}}(1 + iQ_L X)}$$

where $X = \omega/\omega_0 - \omega_0/\omega \approx 2\Delta\omega/\omega_0$ and the loaded cavity quality factor $1/Q_L = 1/Q_0 + 1/Q_{\text{in}} + 1/Q_{\text{out}}$ represents the unloaded quality factor Q_0 of the cavity with external Qs for input and output probes $1/Q_{\text{in}}$ and $1/Q_{\text{out}}$ respectfully. The input and output Qs are defined similarly to the unloaded Q namely

$$Q_{\text{in}} = \frac{\omega U}{P_{\text{in}}} \quad , \quad Q_{\text{out}} = \frac{\omega U}{P_{\text{out}}}.$$

In principle, $\Delta\omega$ follows from the phase shift Φ in S_{21} according to

$$\frac{\Delta\omega}{\omega_0} \approx \frac{1}{2Q_L} \tan\Phi.$$

Using the small angle approximation and a dielectric micarta cylinder ($\epsilon \sim 6$) with $l = 12.7$mm, $r = 6.35$mm for low frequencies and $l = r = 6.35$mm for higher frequencies as the bead perturbation, the magnetic field contribution is negligible resulting in

$$-F_E \frac{\epsilon_0 \mathbf{E}' \cdot \mathbf{E}'^*}{U} = \frac{\Delta\omega}{\omega_0} \approx \frac{\Phi}{2Q_L}.$$

While pulling the bead longitudinally through the cavity, the relative phase is measured inside the cavity. The correlation between bead position and relative phase shift is proportional to the square root of the absolute electric field; $\Phi \propto |E|^2$ as shown above. An example of the longitudinal phase profile of the fundamental mode can be found in Figure 2.2.

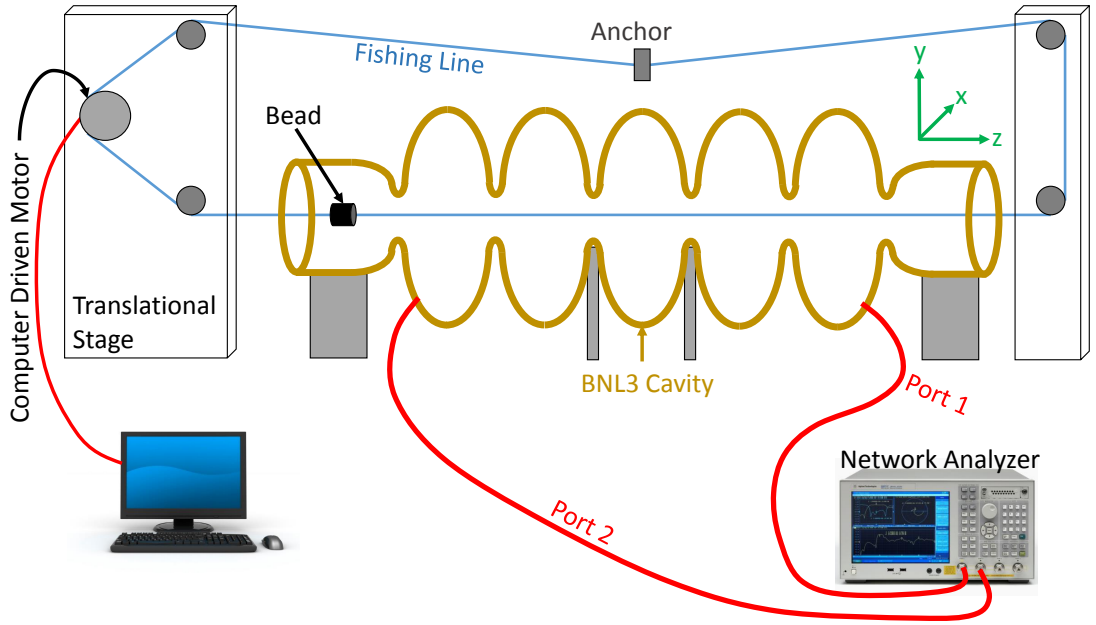

FIGURE 2.1: Schematic of the initial bead pulling assembly for the BNL3 cavity.

2.1.1 Field Flatness Tuning

Measurement and simulation consistency plays a critical role in R&D. While simulation offers a unique insight into construction requirements and tolerances, correspondence between simulation and measurement offers a unique insight into construction errors. Measurement also offers a solution to correct for these errors via limited physical deformation by squeezing or stretching the cavity, also known as field flatness tuning. If possible, this calibration procedure is designed to "level" the field of the π-mode and

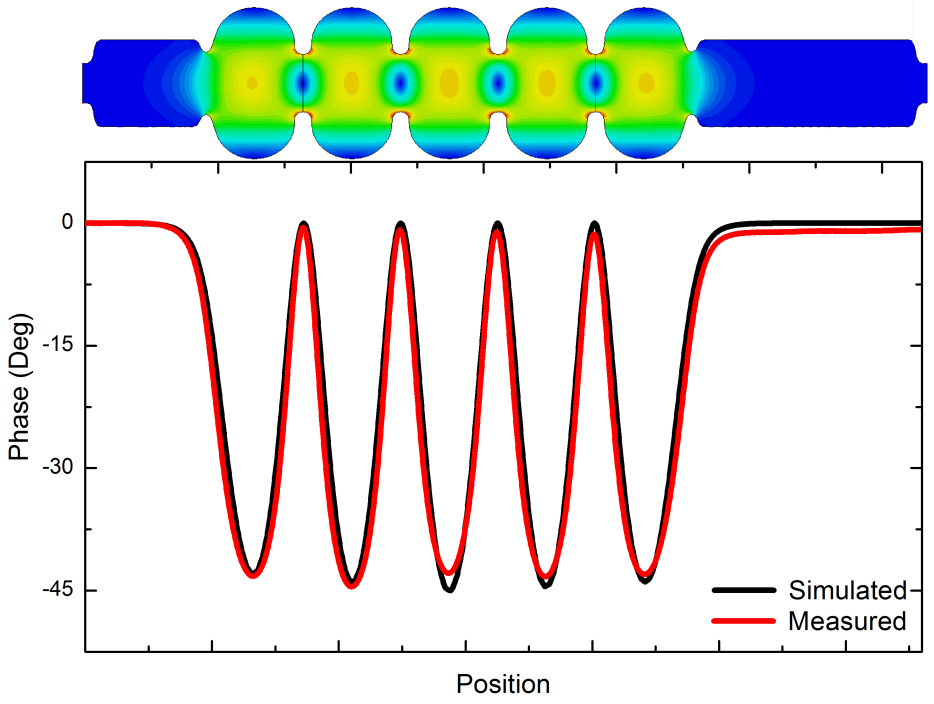

FIGURE 2.2: Longitudinal on-axis phase profile of the π-mode (bottom). The position is directly aligned with the simulated cavity and the simulated absolute electric field profile is also shown (top). The simulated data was normalized with respect to the measured data.

an example of the field flatness of the BNL3 Cu Cavity can be found in Figure 2.2. An approach for such a tuning procedure can be found elsewhere [6].

2.2 HOM Characterization

The initial bead pulling setup, seen in Figure 2.1, was retrofitted with computer controller stepper motors to the manual linear translational stages. This upgrade allows for precision measurements of the azimuthal and radial components of the field distribution relative to the cavity. Having details of the longitudinal, radial and azimuthal components of the field profile yields a comprehensive analysis of HOMs and the field distribution for any open cavity. The upgrade was a natural step towards identification of any trapped modes and correlation between simulation and measurement. The modified assembly can be seen in Figure 2.3. More information about the upgrade can be found in Appendix A.

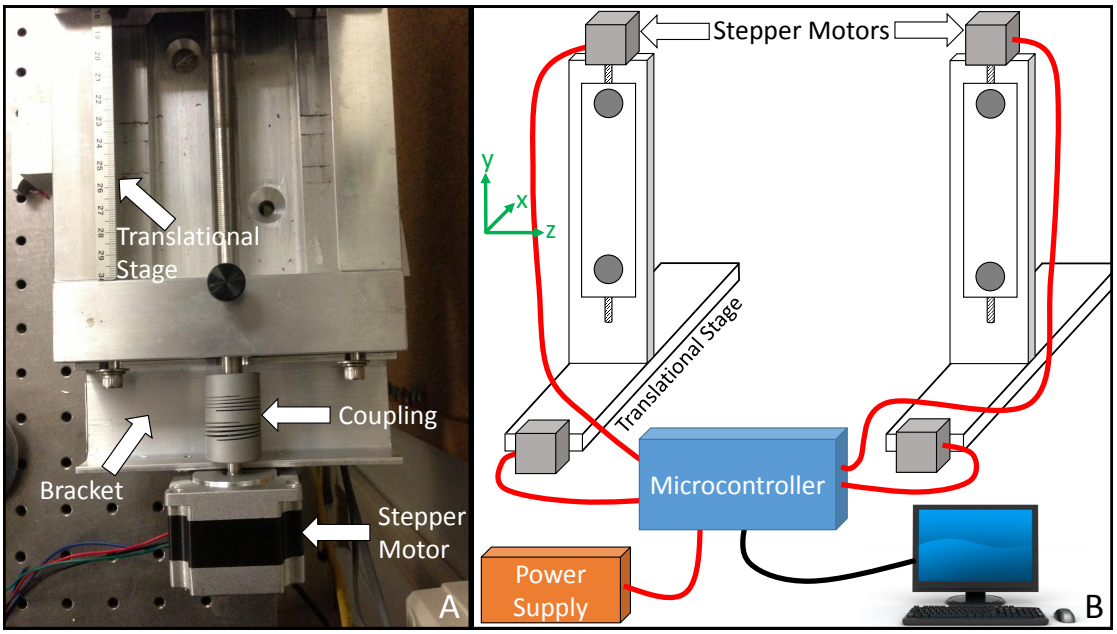

FIGURE 2.3: (A) Picture of necessary equipment for retrofitting the stepper motors. (B) Schematic outlining the improvements on the bead pulling assembly.

2.2.1 Correlation Between Simulation and Measurement

Simulations using CST MWS's Eigenmode solver offers a detailed perspective on the eigenmodes and field distribution of these modes in the BNL3 accelerator cavity. Additionally, MWS handles post processing analysis which yields the quality factor Q_m and R_m/Q_m for each mode. The comparison between measured and simulated Q_m, eigenfrequency and field distribution provides correspondence between simulation and measurement. If the comparison is reasonable then the product between simulated Q_m and R_m/Q_m yields the shunt impedance R_m which is a measure of the strength with which an eigenmode of a resonant RF structure interacts with charged particles. Armed with this information, modes are prioritized by level of hazard, i.e. large R_m values, for future damping criteria. An example comparison of simulated versus measured field distribution of the π-mode can be seen in Figure 2.2 while calculated vs. measured parameters can be seen in Table 2.2. The S_{21} spectrum of eigenmodes associated with the data in Table 2.2 can be seen in Figure 2.4. As an exercise of prudence, the modes with the highest calculated Q_0 values were characterized and correlated to simulation. The results for on-axis measurements for the highest and subsequent highest calculated Q_0 modes in Table 2.2 can be found in Figures 2.5 and 2.6 respectfully. Example azimuthal measurements for the highest and subsequent highest calculated Q_0 modes in Table 2.2 can be found in Figures 2.7 and 2.8 respectfully. These data suggest excellent qualitative agreement with simulation while the quantitative differences could arise from inhomogeneous mode excitation, mode coupling, cavity deformation, coupling to the fundamental

Mode #	Measured GHz	Simulated GHz	Measured Q_L	Simulated Q_0	Simulated R/Q	Mode Type
1	0.70313	0.704850529	32016	41221.071	503.85476	π-mode
2	0.8202799	0.819012561	11800	29441.686	0.011670939	TE Dipole
3	0.8206161	0.819190083	11621	29365.62	0.010257734	TE Dipole
4	0.8277265	0.825313726	15081	30614.425	0.17589805	TE Dipole
5	0.8282307	0.825484847	9938	30499.172	0.18300436	TE Dipole
6	0.8414034	0.84122939	5340	31998.071	0.004157926	TE Dipole
7	0.8417508	0.841423927	6304	31910.012	0.004184892	TE Dipole
8	0.858886	0.859344189	7160	34155.692	0.030851596	TE Dipole
9	0.8588896	0.859444724	<1000	34098.655	0.03015289	TE Dipole
10	0.8838738	0.882570241	3278	35647.863	0.25457567	TE Dipole
11	0.88434521	0.882746489	4582	35533.717	0.26064527	TE Dipole
12	0.914981	0.914578312	5344	36327.482	0.000845256	TE Dipole
13	0.9150147	0.914713839	<1000	36233.937	0.001107484	TE Dipole
14	0.9423829	0.944787131	6940	32167.241	0.45099498	TM Dipole
15	0.9424068	0.944935239	2716	32123.819	0.45684639	TM Dipole
16	0.975525	0.976194409	3241	49033.747	0.000744925	TM Dipole
17	0.9768923	0.976222841	1163	48970.065	0.000921287	TM Dipole
18	1.00346	1.00483075	<1000	47650.756	0.25275407	TM Dipole
19	1.011896	1.01498	6027.3	49136.81	0.26006942	TM Dipole
20	1.018852	1.02212	13990	50570.75	0.20714834	TM Dipole

TABLE 2.2: Tabular data of the first few measured and simulated modes above the fundamental mode in the BNL3 cavity. R/Q was calculated 1cm away from beam axis.

power coupler and/or HOM antenna, lack of simulated cavity components, etc. Nevertheless the quantitative differences are relatively small indicating the simulated values of eigenmode frequency, Q_m and R_m/Q_m are realistic.

2.2.2 Split Mode Observations

The BNL3 Cu cavity can be excited such that "split" mode resonances are observed. Split modes are degenerate modes that have a relative polarization $\pi/2$ out of phase from each other and are common in superconducting cavities. The bead perturbation measurement can distinguish between polarizations and an example of a measured quadrupole split mode can be seen in Figure 2.9. The importance of discovering the polarization is owed to the fact that HOM couplers couple to the local field and therefore anticipation of the field location is critical for correct HOM coupling location briefly discussed in Section 1.3.4. The bead perturbation measurement is sensitive enough to differentiate between monopoles, dipoles, quadrupole and even sextupoles. An example

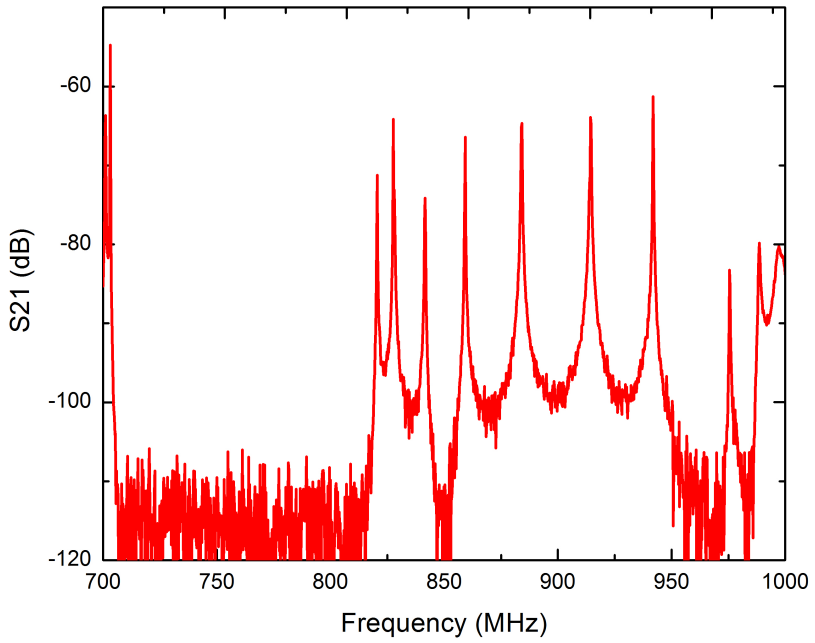

FIGURE 2.4: S_{21} spectrum of the modes taken from Table 2.2. Probes used for excitation and measurement were located in cells 1 and 5 respectfully.

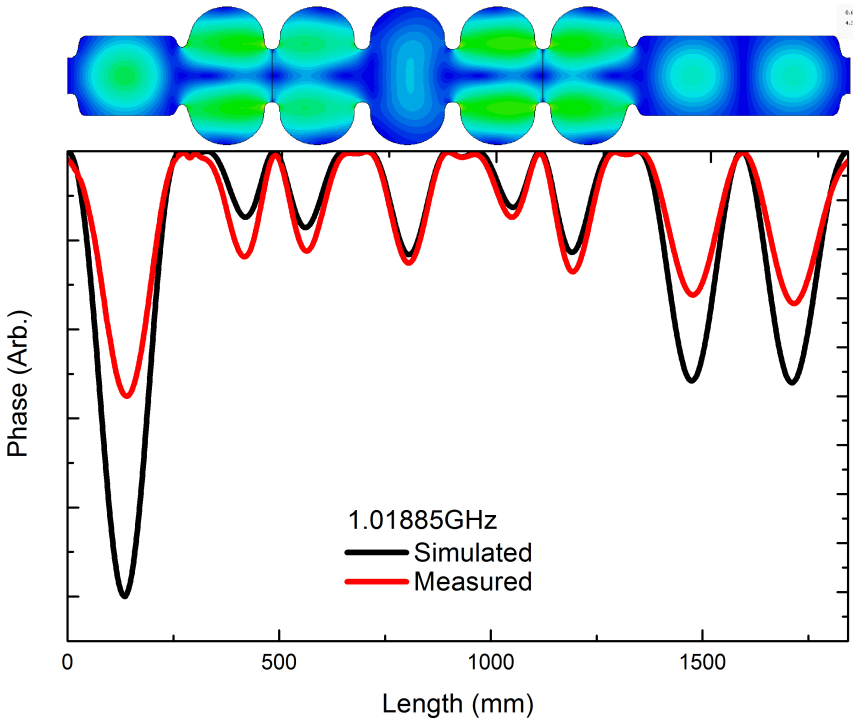

FIGURE 2.5: On-axis longitudinal phase profile of the highest simulated Q_0 mode in Table 2.2. The top figure is the simulated field profile of the BNL3 cavity which is aligned with the abscissa.

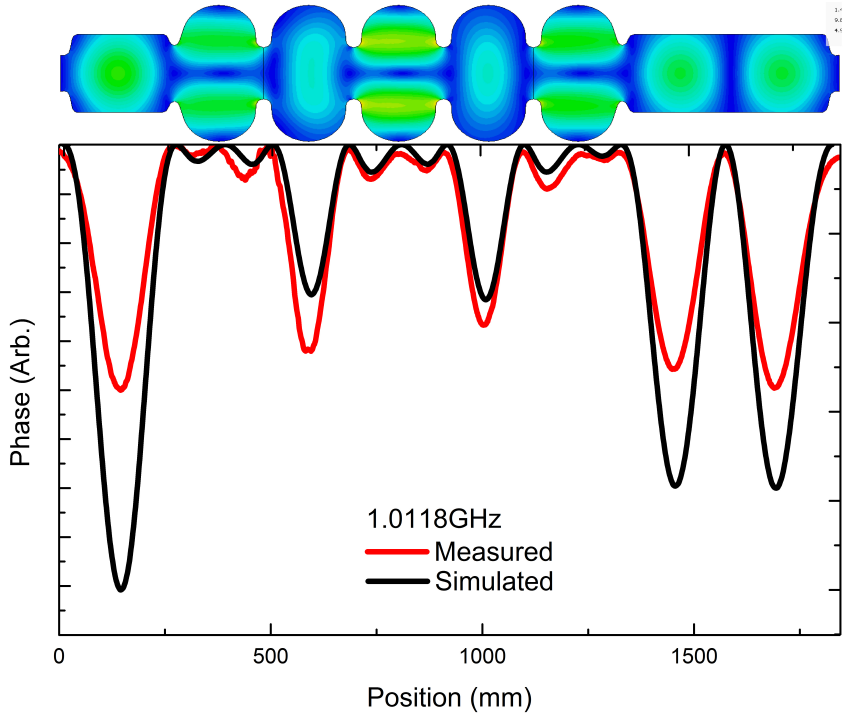

FIGURE 2.6: On-axis longitudinal phase profile of the subsequent highest simulated Q_0 mode in Table 2.2. The top figure is the simulated field profile of the BNL3 cavity which is aligned with the abscissa.

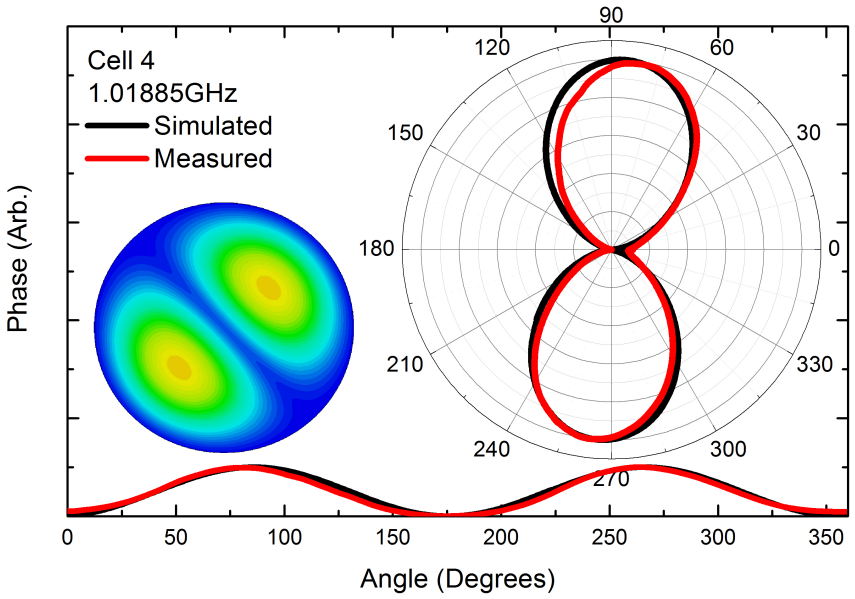

FIGURE 2.7: Azimuthal phase profile 4cm off axis of the highest simulated Q_0 mode in Table 2.2. The insets are the simulated cross section of the electric field profile of Cell 4 (left) and the representative data as a radial plot (right).

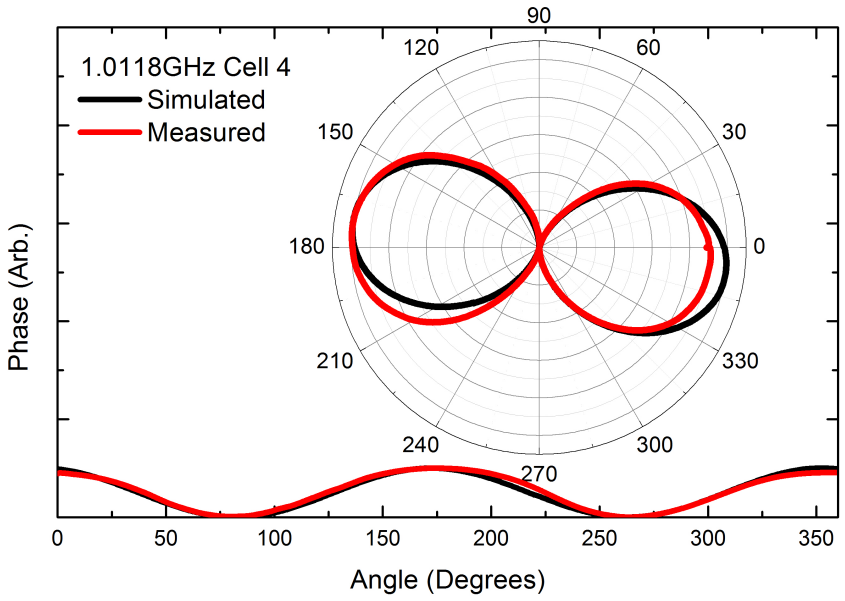

FIGURE 2.8: Azimuthal phase profile 4cm off axis of the subsequent highest simulated Q_0 mode in Table 2.2. The inset is the representative data as a radial plot.

measurement of a bona fide sextupole can be seen in Figure 2.10. At this scale the thermal and mechanical fluctuations start to provide a significant background signal and compensation of the background is necessary. For an accurate field profile measurement a polynomial background was subtracted off from the raw data.

2.2.3 TE and TM Mode Differentiation

The distinction between TM and TE modes is important when evaluating the dangers associated with HOMs as discussed briefly in Section 1.3. TE modes have no on-axis electric field hence the beam cannot excite these modes and therefore pose little threat in disrupting the beam. On the other hand TM HOMs not only act to accelerate and decelerate the beam but could also be excited to deflect the beam. Since TEM and hybrid modes are forbidden in the BNL3 cavity the differentiation of TM and TE modes is possible with the guidance of simulation and characterization. Looking at Figures 2.9 and 2.10 the blue contour represents a minimum in the electric field while red represents a maximum. The boundary conditions associated with this contour plot suggests either the presence of an electric field or not. The Dirichlet and Neumann boundary conditions discussed in Section 1.3 impose that if there is an electric field present on the boundary then the electric field must be directed towards the boundary and suggests a TE mode

while the absence of the field on the boundary a TM mode. Hence the electric field profiles in Figures 2.9 and 2.10 suggest TE and TM modes respectfully.

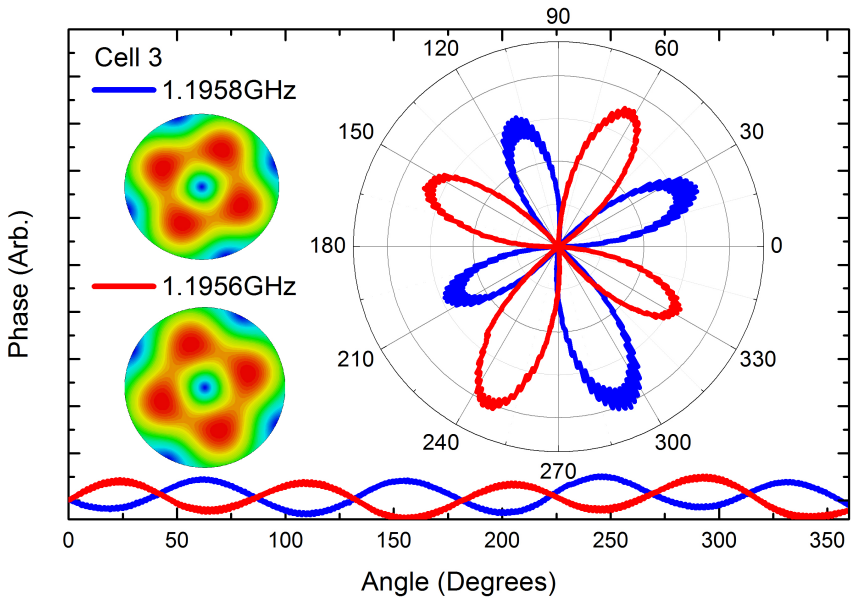

FIGURE 2.9: Azimuthal phase profile 4cm off axis of quadropole split modes centered around 1.1957GHz. The insets on the left represent the simulated cross sectional field profile of the modes where the representative data as a radial plot on the right.

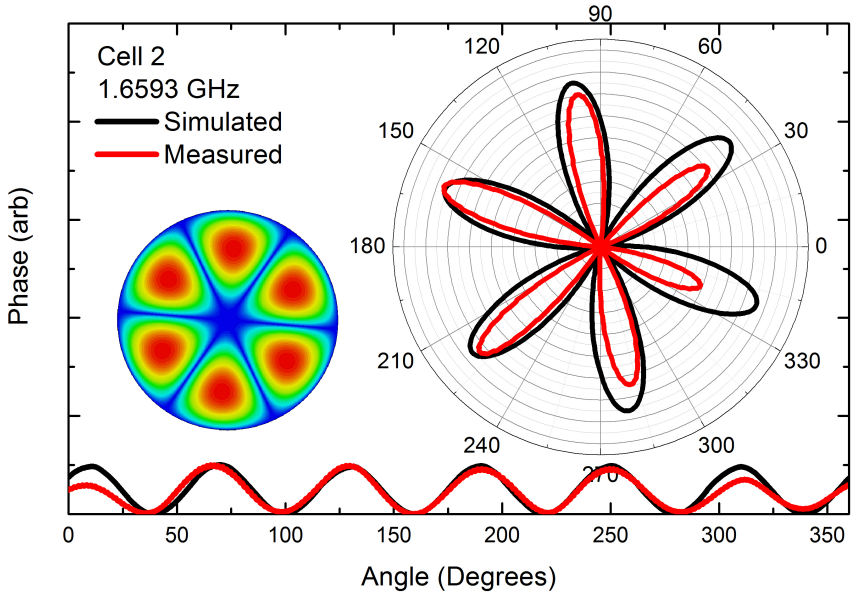

FIGURE 2.10: Azimuthal phase profile 4cm off axis of a sextupole mode minus a background contribution. The insets are the simulated cross section of the electric field profile of Cell 2 (left) and the representative data as a radial plot (right).

Chapter 3

Crab Cavity Measurements

The following chapter discusses the next step for the Large Hadron Collider (LHC) and an example technology known as crab cavities to realize this next step. This cavity was evaluated using our measurement system to ensure proper operation and correlation of HOMs from simulation and measurement.

3.1 Introduction

The LHC is underway for a major upgrade to increase its luminosity by an order of magnitude beyond its original design specifications. The novel machine configuration known as the High Luminosity LHC (HL-LHC) will rely on various innovative technologies including very compact and ultra precise superconducting crab cavities for beam rotation[20]. Implementation of a non-zero crossing angle at the interaction region alleviates parasitic collisions and permits the largest number of bunches. However luminosity is lost from a non-zero crossing angle due to the geometric factor of the rotated bunches. To remedy the rotation a transverse deflection from a crab cavity (CC) aligns the bunches for a head-on collision and is subsequently rotated back before entering the accelerator for normal operation. A schematic drawing outlining the idea of crabbing can be seen in Figure 3.2. A prototype deflecting cavity for the HL-LHC was commissioned and can be seen in Figure 3.1 alongside its simulated model.

3.2 Crabbing Mode Analysis

As mentioned above, a transverse kick is needed to properly align the bunches in order to preserve luminosity. The transverse kick is delivered to the bunch using the so called

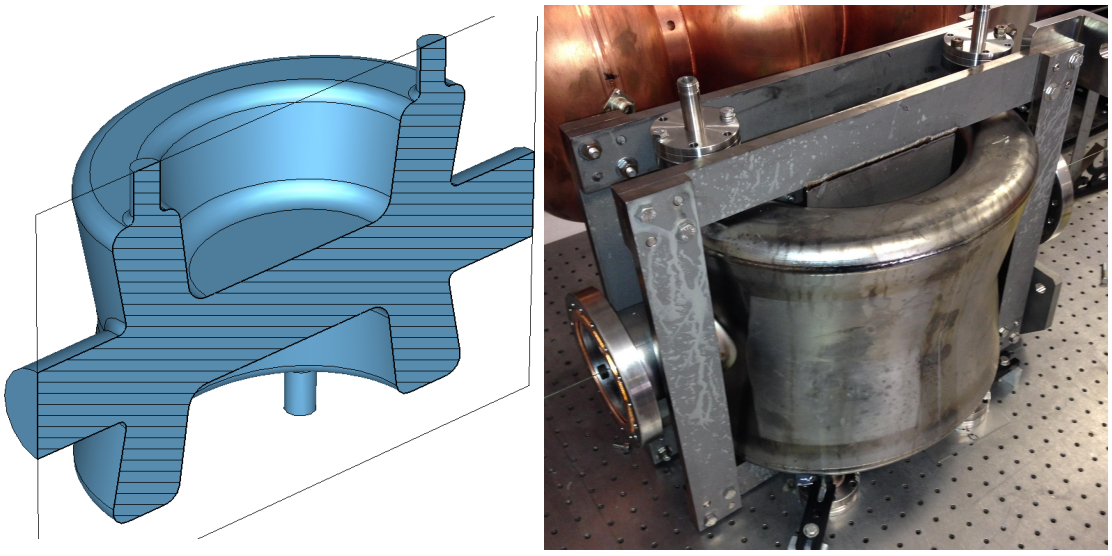

FIGURE 3.1: Cross sectional view of the simulated CC design for the HL-HLC upgrade (left). Photograph of the niobium prototype CC manufactured for the HL-HLC upgrade surrounded by a stiffening frame (right).

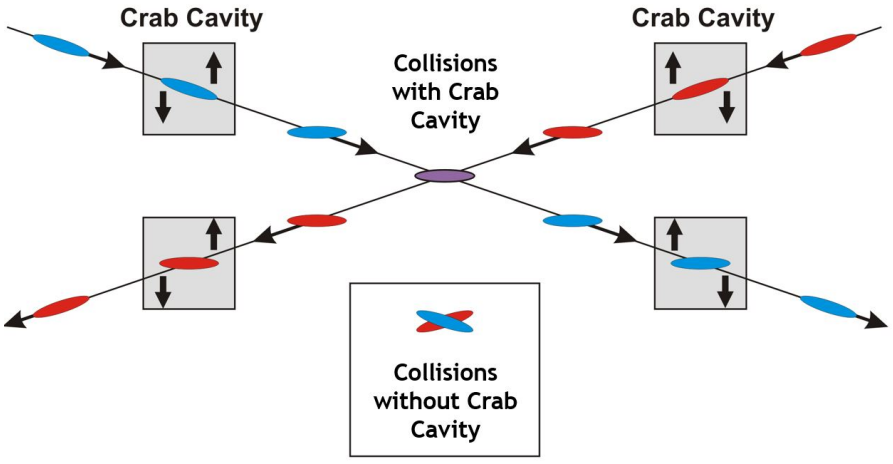

FIGURE 3.2: Artist's rendition of the principles behind a non-zero crossing angle and the use of crab cavities to align electron bunches for head-on collisions.

"crabbing mode". The geometry of the CC allows for a magnetic field vortex similarly discussed in Section 1.3 but where the vortex is now aligned perpendicular to the beam. The crabbing mode and bunch are synchronized when the bunch is located at the center of the cavity and the mode at the zero crossing of the time varying RF power. Since the center of the bunch is at the zero crossing of the RF power it experiences no deflection while the head and tail of the bunch are kicked in opposite directions. Quadruple focusing magnets are used to prevent the bunches from continuing its deflection and reach the interaction point aligned. To ensure proper operation we have used our HOM characterization assembly to analyze the off-axis electric field distribution about the center of the CC. The cavity was aligned with respect to the bead pulling assembly by centering the fishing line with respect to the beam tube flanges and leveling the

cavity with respect to the optical table/bead pull assembly. Having a relatively large micarta bead compared to the CC could perturb the eigenmode such that the small angle approximation discussed in Section 2.1 is violated. Therefore several beads were constructed with teflon ($\epsilon \sim 2$) and various geometries that could be substituted to justify the small angle approximation. The longitudinal measurement of the off-axis field profile of the crabbing mode was carried out in 1mm steps with a cylindrical micarta bead with dimensions of a 4mm radius by 1.5mm thick. This geometry provided the best signal to noise ratio without violating the small angle approximation. The results of this scan can be seen in Figures 3.3 and 3.4. Each individual longitudinal scan was fitted with its simulated counterpart resulting in an average $\chi^2 = 0.0447$ and $\chi^2 = 0.0463$ for the horizontal and vertical configurations respectfully. Yielding a probability that the simulated model reflects the measurement ($P_\chi(\chi^2;\nu)$) by over 93% and 92% for the vertical and horizontal configurations respectfully using only $\nu = 2$ degrees of freedom namely a proportionality constant and an offset to relate the simulated results to the data. The $\sim 10\%$ discrepancy is consistent with the uncertainty of the CC alignment and mechanical survey.

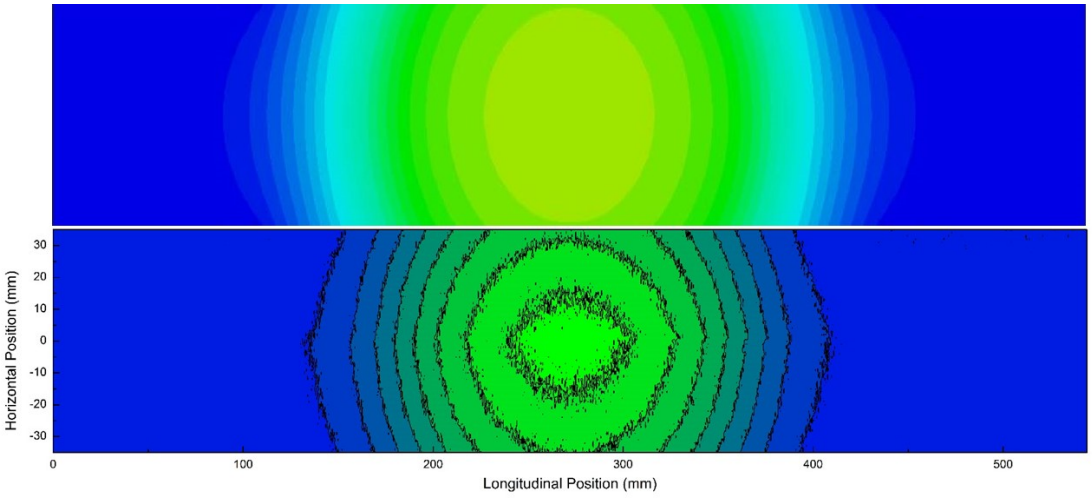

FIGURE 3.3: Top and bottom figures represents the simulated and measured contour plot of the absolute electric field profile of the crabbing mode parallel to the capacitive plates. The lowest to highest field is represented by blue to green colors respectfully.

3.3 HOMs

Unlike the BNL3, the geometry of the CC allows for TEM modes. The hollowed sides leading into the cavity center displayed in Figure 3.1 act like capacitive plates and consequently an inner conductor. HOMs up to 2GHz were investigated in the CC using the bead pulling assembly from Figure 2.1 and a summary of the investigation for the first fifteen HOMs can be seen in Table 3.1. For brevity, only analyses performed on the

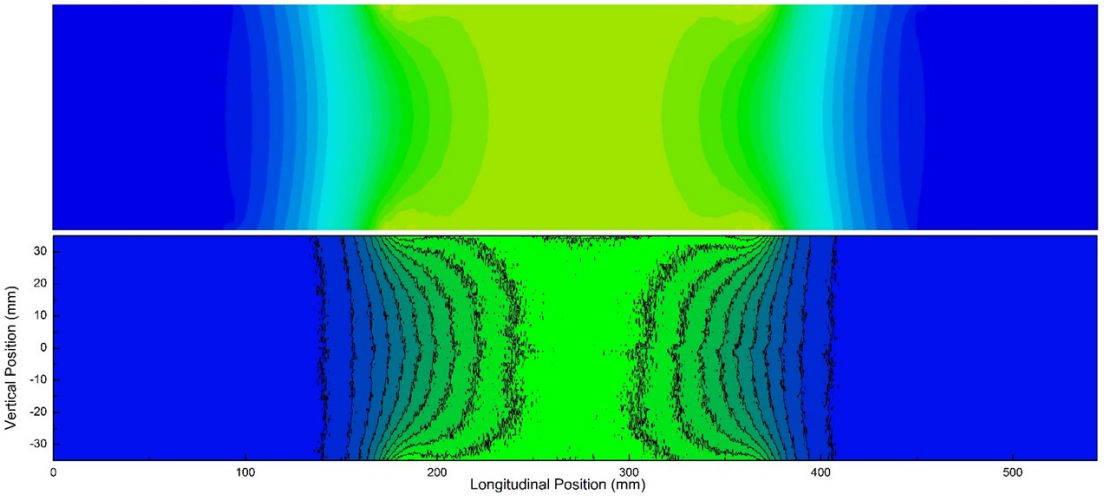

FIGURE 3.4: Top and bottom figures represents the simulated and measured contour plot of the absolute electric field profile of the crabbing mode perpendicular to the capacitive plates. The lowest to highest field is represented by blue to green colors respectfully.

TM dipole located at 1.952GHz were shown, however similar analyses were performed for all HOMs up to 2GHz. Longitudinal measurements of the electric field profile were performed on axis and 2cm off axis both in the x and y plane of the CC and correlated with simulated results as shown in Figure 3.5. Azimuthal scans 2cm from the beam axis were also measured both at the center of the CC and a quarter of the total length inside the CC. Figure 3.6 shows the azimuthal scan a quarter of the total length into the CC of the TM dipole mode located at 1.952GH and notably the field profile is asymmetric as indicated by both the measurement and simulation. The asymmetric port locations on the CC could explain this result.

All measurements were consistent with the simulated model results. These results suggest a reassurance of the CC's performance and predictability as well as the validation of subsystem component functionality namely the fundamental power coupler and the pickup probe.

Mode #	Measured MHz	Simulated MHz	Mode Type
1	403.27	397.04	Crabbing
2	580.27	576.32	TM Dipole
3	675.37	670.07	TEM Dipole
4	703.83	698.71	TM Dipole
5	755.65	752.22	TEM Dipole
6	803.5	799.94	TE Quadruple
7	920.56	915.32	TEM Dipole
8	956.93	946.8	TM Dipole
9	1080.83	1077.89	TEM Dipole
10	1104.37	1101.94	TE Quadruple
11	1118.31	1113.86	TEM Dipole
12	1211.25	1202.35	TEM Dipole
13	1258.31	1246.63	TM Dipole
14	1296.19	1290.51	TEM Dipole
15	1358.12	1352.36	TE Dipole
16	1414.68	1408.36	TE Quadruple

TABLE 3.1: Tabular data of the first few measured and simulated modes above the crabbing mode in the HL-LHC CC.

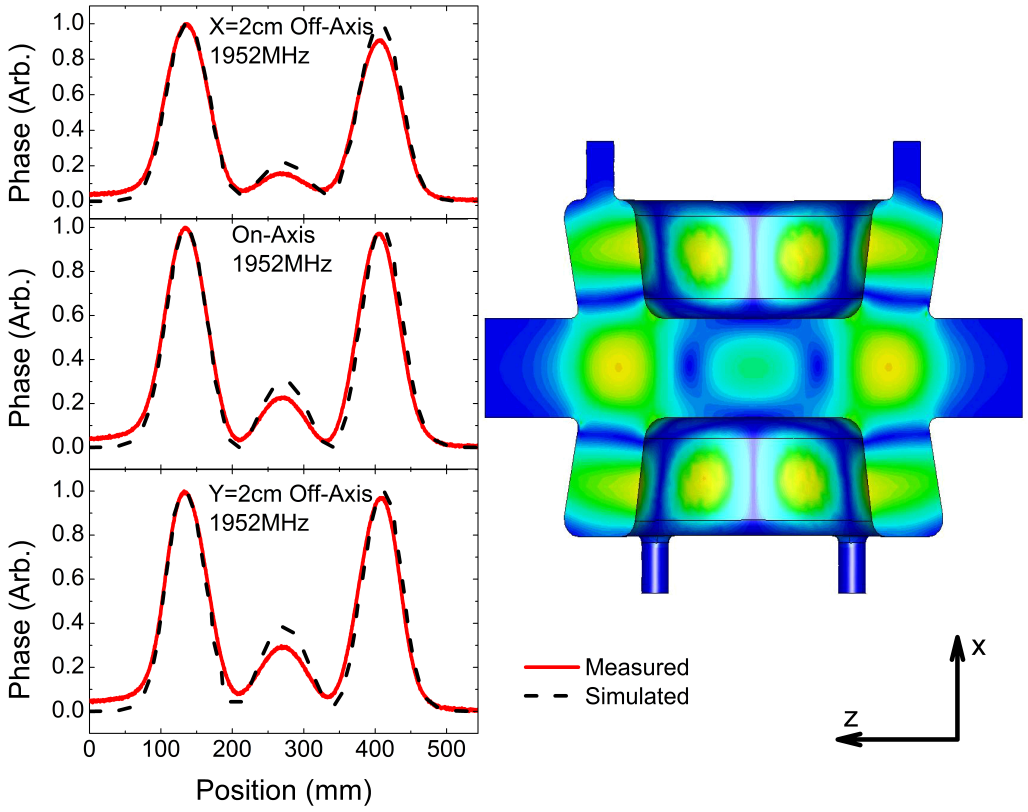

FIGURE 3.5: The left shows CC analyses performed both on and 2cm off axis in the x and y plane while the right shows the simulated electric field profile cross section of the TM sextupole mode located at 1.952GHz.

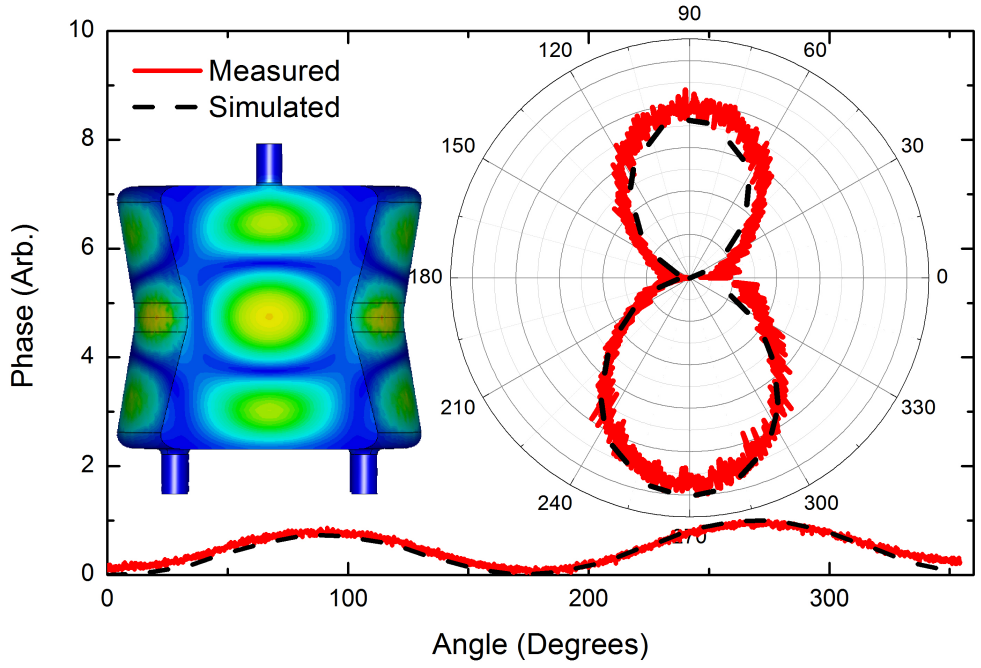

FIGURE 3.6: Azimuthal scan 2cm off axis and a quarter of the total length into the CC of the TM sextupole mode located at 1.952GHz. Insets show the radial plot of the normalized data and the cross section of the electric field profile a quarter of the total length inside the CC.

Chapter 4

Coaxial to Dual-Ridge Waveguide Design

The following chapter outlines the process for developing a HOM coupler for the BNL3 linac. Several designs schemes were evaluated with unsatisfactory results. For brevity, only a few of these designs will be shown for comparison.

4.1 Benchmark Design Considerations

Having already analyzed a coaxial HOM coupler in the BNL3 cavity, any future coupler considerations would have to meet or exceed the transmission performance S_{21} shown in Figure 1.10. A coaxial to waveguide design would give juxtaposition between a waveguide and lumped circuit design and could serve as a solution for HOM damping. HOM coupler geometry, assembly and implementation were all key factors in the design process. Mechanical and thermal tolerances that impact cut-off frequency and S_{21} robustness was also a concern.

4.1.1 Dual Ridge Waveguide

Rectangular WG functionality was briefly discussed in Section 1.3.4. Adding ridges to the rectangular WG offers advantages such as a lower cutoff frequency f_c, greater attenuation, compact cross section, greater HOM separation and lower impedance. A ridge can also be a foundation for a coaxial counter part or a channel for a cryogenic/water cooling network, more on this in the proceeding section. The cutoff frequency f_c for a dual-ridged (DR) WG can be approximated by the following formula

Parameters (mm)	
g	5
h	35
l	32
d	11

TABLE 4.1: Relevant DR WG Parameters.

$$f_c = \frac{1}{2\pi\sqrt{\mu\epsilon}}\sqrt{\frac{g}{hld}}$$

where the relevant physical parameters can be seen in Figure 4.1 while the parameters used for the actual WG after optimization are given in Table 4.1 [16, 21]. Many geometric configurations will give the same cutoff frequency, an example transmission spectrum for similar DR WGs with cut-off frequency set to the first HOM of the BNL3 cavity (820MHz) can be seen in Figure 4.2. Having a cut-off frequency set to the first HOM ensures the propagation of all HOMs and the attenuation of the fundamental mode. The mode separation between the fundamental and the first HOM as well as the overall length of the WG attenuates the fundamental exponentially, the quantum mechanical equivalent to tunneling. These phenomena can be seen in Figure 4.2.

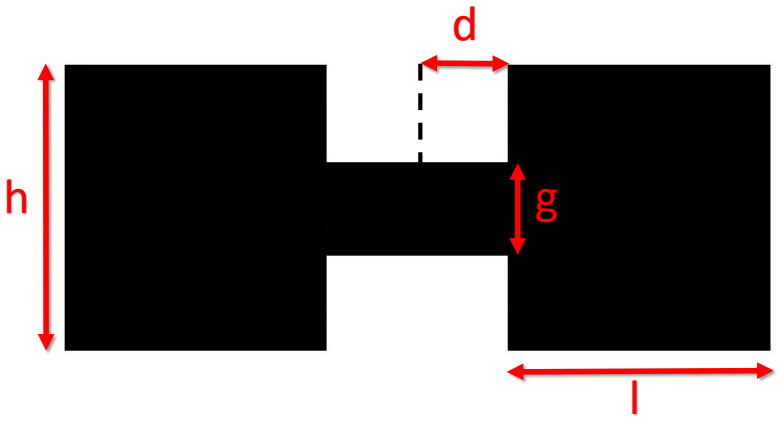

FIGURE 4.1: Cross sectional view of a DR WG and relevant physical parameters.

The overall geometry of the DR WG was chosen to support a cut-off frequency at the first HOM while eliminating standing waves or resonances inside the WG below 4GHz. The corresponding wavelength for 4 GHz is 37.5mm and indeed the longest cross sectional dimension of the DR WG does not exceed this limitation. An expected resonance is to occur around 4.28GHz from the 35mm dimension of h which will interfere with the transmission of HOM power out of the cavity due to 35mm standing wave trapped inside the WG. However R/Q values above 3GHz are expected to be well below

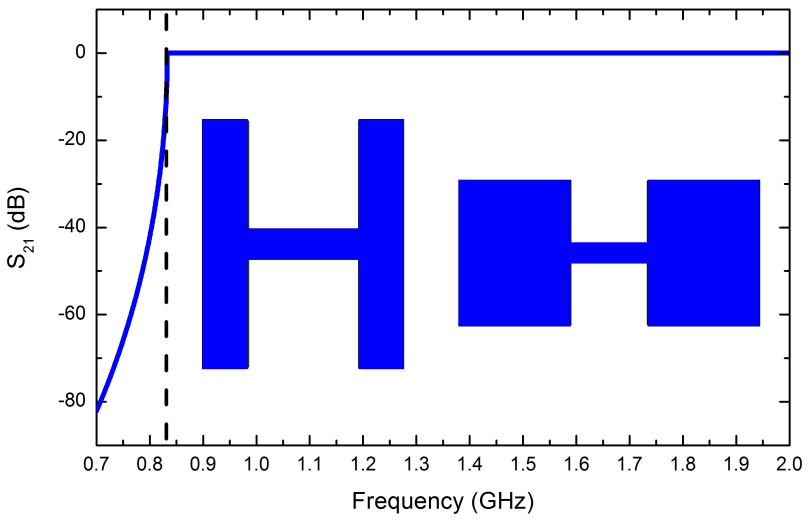

FIGURE 4.2: Simulated S_{21} transmission of the idealized 1m long DR WG insets. The dashed line represents the first HOM for the BNL3 cavity while the inset represents the cross-sectional area of the DR WGs.

threshold for BBU and mode power above this range is expected to propagate out to the cavity end tubes. If necessary, trapped power inside the DR WG can be extracted by conventional means such as coating the DR WG walls with ferrite dampers. The optimized DR WG design cuts the cross sectional area from its rectangular WG brother by a staggering 87% which can be seen in Figure 4.3.

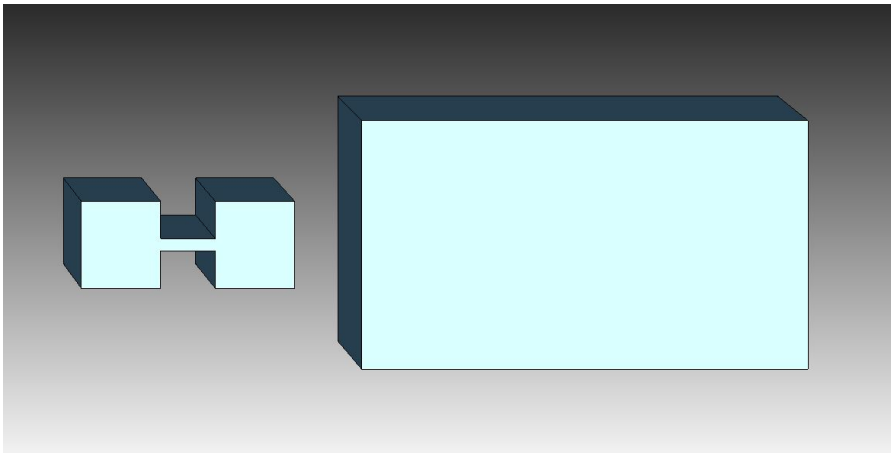

FIGURE 4.3: Cross sectional comparison between the DR WG design to its cut-off frequency equivalent Rectangular WG.

4.1.2 Coaxial Interconnect

Using a coaxial line to extract unwanted power from the accelerator cavity to the WG coupler would offer several advantages over a conventional waveguide. An N-type RF connector would provide a standard 50Ω impedance which would simplify future matching criteria, offer a broad spectrum passband of DC power up to 18GHz and is physically flexible. Using a coaxial line allows flexibility over WG orientation and placement with respect to the accelerator cavity, alleviating some constraints on the cryomodule. Additionally, once an interconnect (IC) between coaxial line to DR WG is established the problem of extracting power from the WG to an outside RF load is solved since the scatter matrix components S_{21} and S_{12} are identical for a lossless transmission line. The challenges associated with designing an IC is impedance matching or tuning so that no HOM power is reflected back into the cavity while eliminating parasitic reactance of TEM-TE mode conversion. The theory of small reflections provides an idea of how to solve the problem of impedance matching. By using so called multisection transformers, mode propagation from one section to another is possible without reflection in a specified passband [7]. An attempt to make a smooth transition having $N \to \infty$ sections from coaxial to DR WG can be seen in Figure 4.4 where one of the ridges from the DR WG is used as a foundation for the coaxial antenna. However with this design attenuation of frequencies well above the DR WG cut off frequency was observed due to the fact that the DR WG dimensions are decreasing approaching the coaxial line.The length of the IC was comparable to the DR WG itself and not to mention the construction of such an IC is challenging.

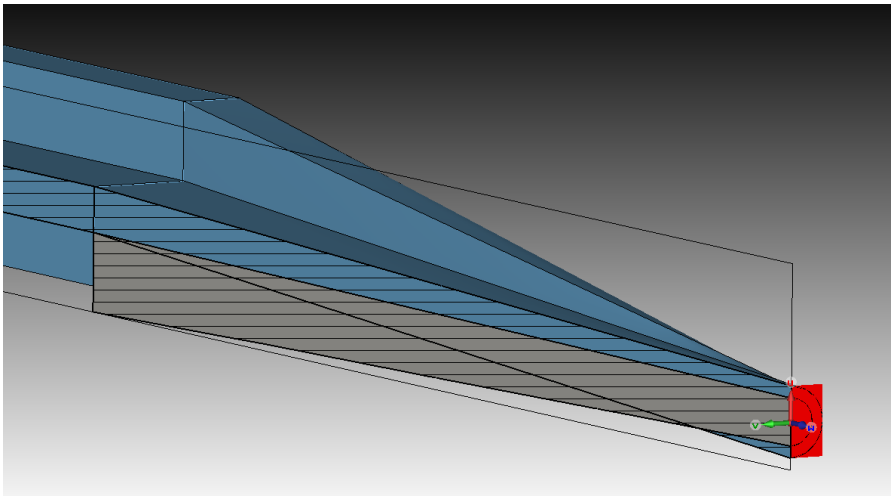

FIGURE 4.4: Cross section of a simulated coaxial to DR WG IC with $N \to \infty$ sections.

A different approach was carried out using a four section HOM coupler from the cavity to the DR WG and are outlined in Figure 4.5. These four sections have two purposes namely mode conversion of TEM modes from the coaxial line to compatible

TE modes in the DR WG and impedance matching. A rectangular-circular coaxial portion has been investigated to increase bandwidth and has been used in this design to redistribute the electromagnetic field focused from the coaxial aperture to the single ridge coaxial portion. A capacitive stub in the single-ridge coaxial line provides distribution of the parasitic inductance and as a result provides a more effective broad-band mode conversion [22].

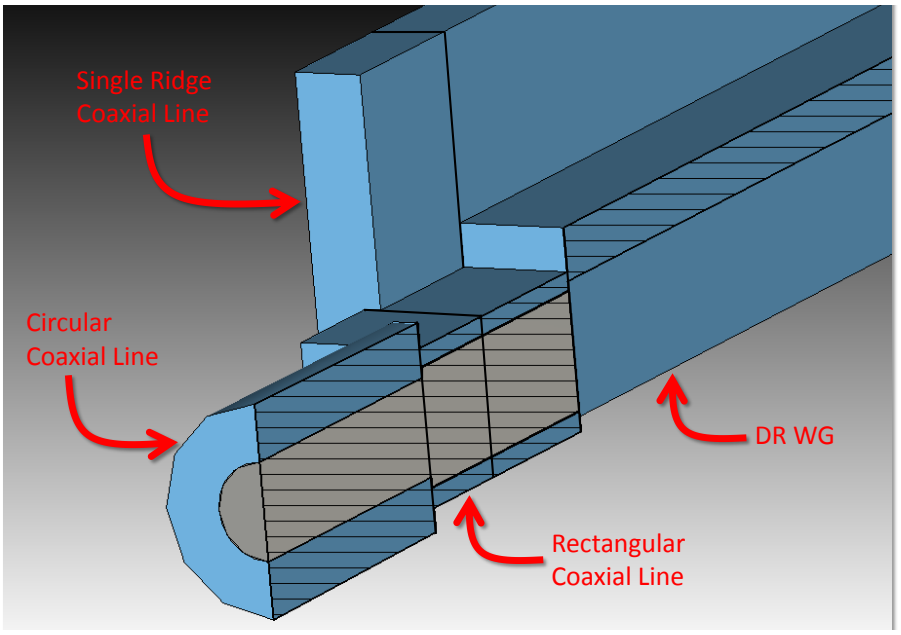

FIGURE 4.5: Cross section of a simulated four section IC design.

4.2 Simulations

Frequency domain simulations in CST provided insight on the impedance matching criteria and the RF performance of the structure. A typical simulated transmission spectrum of a preliminary HOM coupler can be seen in Figure 4.6. The sharp linewidth-like features in the S_{21} simulation correspond to cut-off frequencies associated with having the DR WG as a terminated WG port with one specified mode of propagation. These features can be shifted or eliminated by either changing the geometry of the DR WG or by introducing more modes of propagation to the WG port. Having set the DR WG geometry to the parameters given in Table 4.1 the first cut-off frequency was shifted to 4.28 GHz, however the broad features remaining correspond to the fundamental mode rejection and the impedance mismatch of the design. The parametrization of coupler dimensions accelerated the optimization process and impedance matching yielding the optimized structure in Figure 4.7 and its transmission in Figure 4.8. The oscillations in the S_{21} transmission spectrum in Figure 4.8 correspond to standing waves inside a one

meter long DR WG with coaxial ICs on either ends. From Figure 4.8 we can see that the Coaxial to DR WG outperforms the two stage coaxial coupler seen in Figure 1.9 with respect to RF transmission above 825MHz as well as the rejection of the fundamental mode. Having a relatively simple design criteria and an impressive RF transmission this design was considered for fabrication.

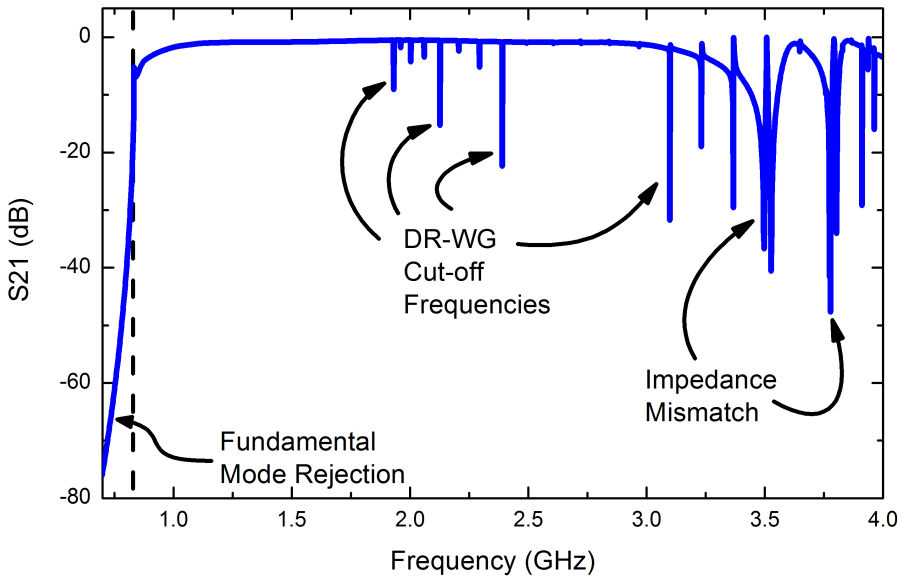

FIGURE 4.6: Simulated preliminary HOM coupler transmission.

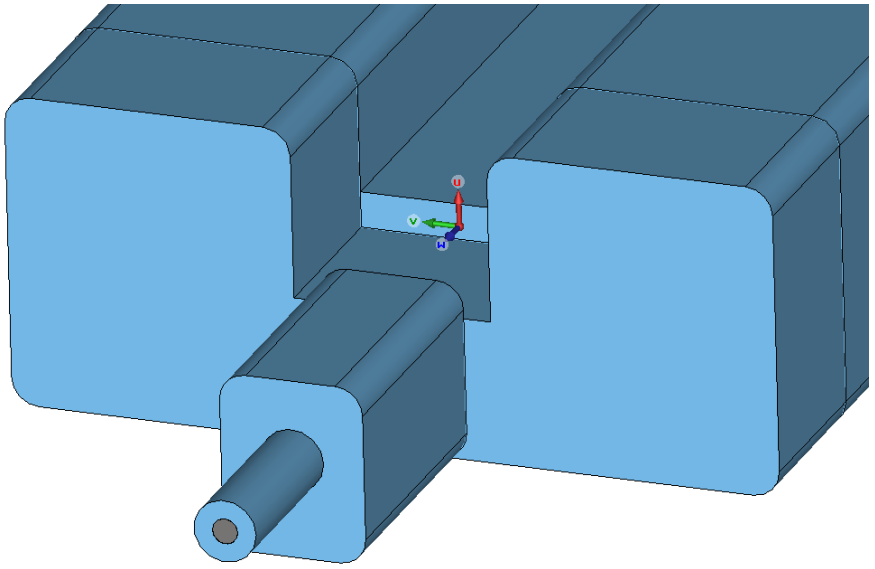

FIGURE 4.7: Simulated optimized HOM coupler IC.

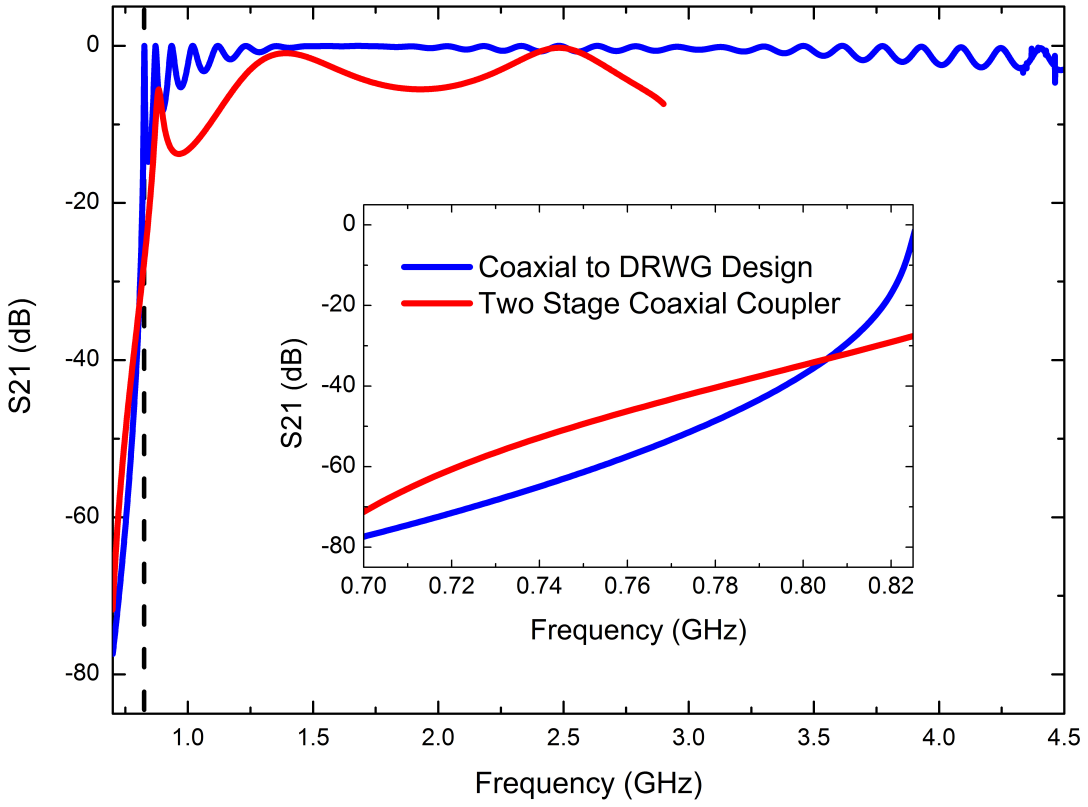

FIGURE 4.8: Simulated transmission for the optimized HOM coupler design as compared with the two stage coaxial coupler. The dashed line represents the first HOM while the initial abscissa value is 703MHz. The inset represents data from the fundamental mode to the first HOM.

4.3 Final Design Considerations

Many manufacturing and measurement concerns were taken into account before releasing the final design for fabrication. An example can be seen in Figure 4.7 where the rounded DR WG edges simulate the WG geometry after peripheral milling. To avoid potential reflections and resistive losses at the joints caused by a faulty seal a lip at the point of contact of the DR WG flanges was added along with dowel pins to ensure a proper seal and alignment which can be seen in Figure 4.9.

The proof of principle HOM coupler transmission will be investigated using two N-type RF connectors on both ends of the HOM coupler which are then connected to a network analyzer for evaluation of the RF transmission performance. The final coaxial interconnect design will incorporate both an N-type RF connector and a cavity flange connector which is impedance matched to the BNL3 cavity. The N-type RF connector assembly can be found in Figure 4.10 which is fixed to the coaxial IC and a set screw attaches the IC antenna to the N-type antenna. The IC antenna is connected to the

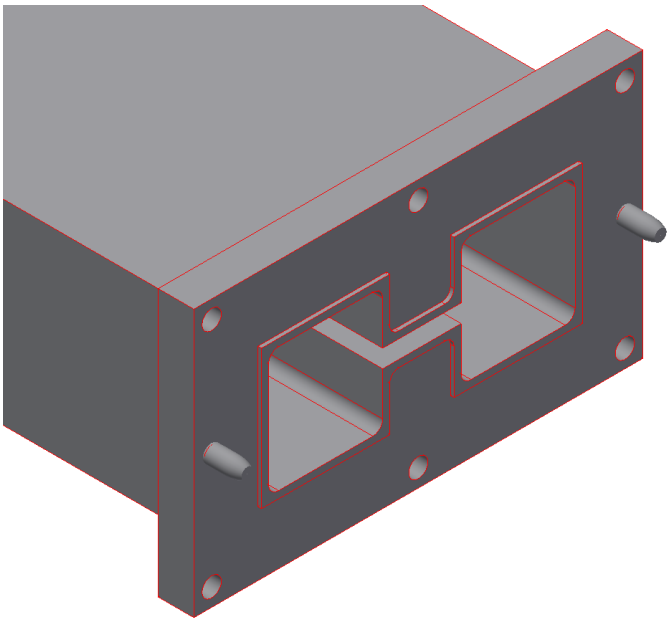

FIGURE 4.9: CAD rendering of the optimized DR WG with highlighted lip and alignment pins.

edge of the DR WG using a gold plated multilam plug for excellent electrical contact and support. The N-type antenna assembly as a whole can be seen in Figure 4.11 while a cross section of the integrated N-type antenna assembly to the HOM coupler can be seen in Figure 4.12. The cavity side IC can be seen in Figure 4.13 where the IC antenna is now supported using a 1.5mm thick teflon bracket which is relatively transparent in the RF spectrum as well as a gold plated multilam plug. The cavity side IC antenna is intended to have a female connector for future antenna end geometry design.

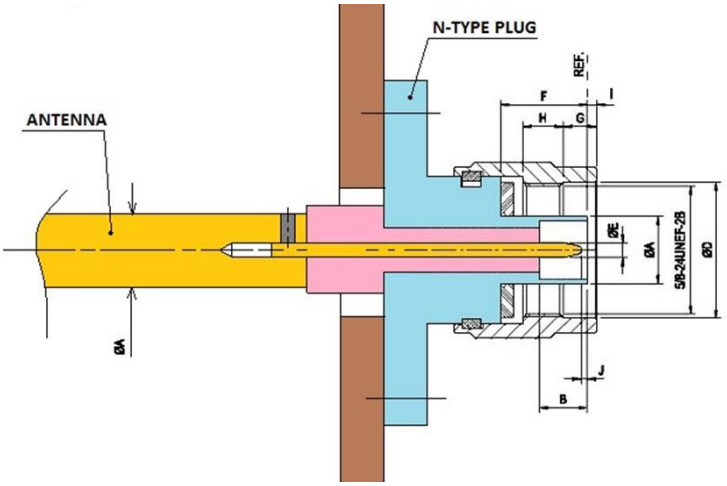

FIGURE 4.10: N-type RF connector assembly schematic.The pink and brown components are teflon and the IC face respectfully.

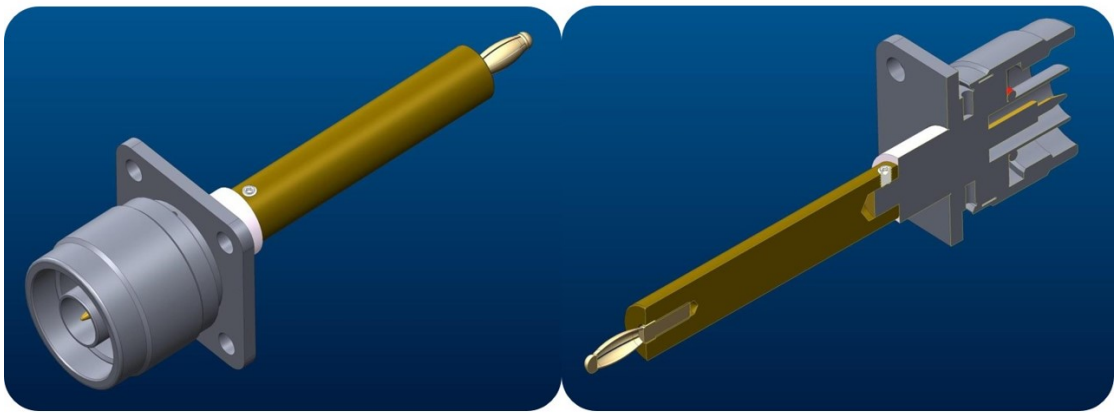

FIGURE 4.11: Antenna assembly schematic with a gold plated multilam plug electrically connecting the antenna to the DR WG.

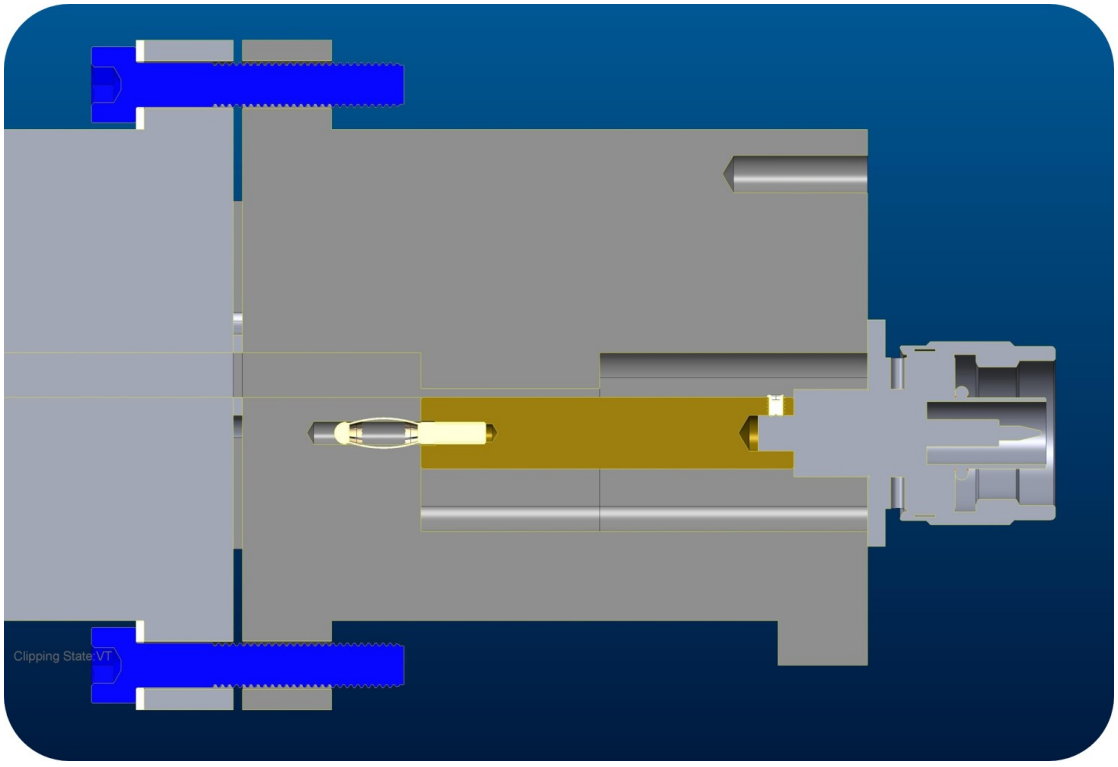

FIGURE 4.12: Cross sectional view of the antenna assembly attached to the DR WG and N-type connector.

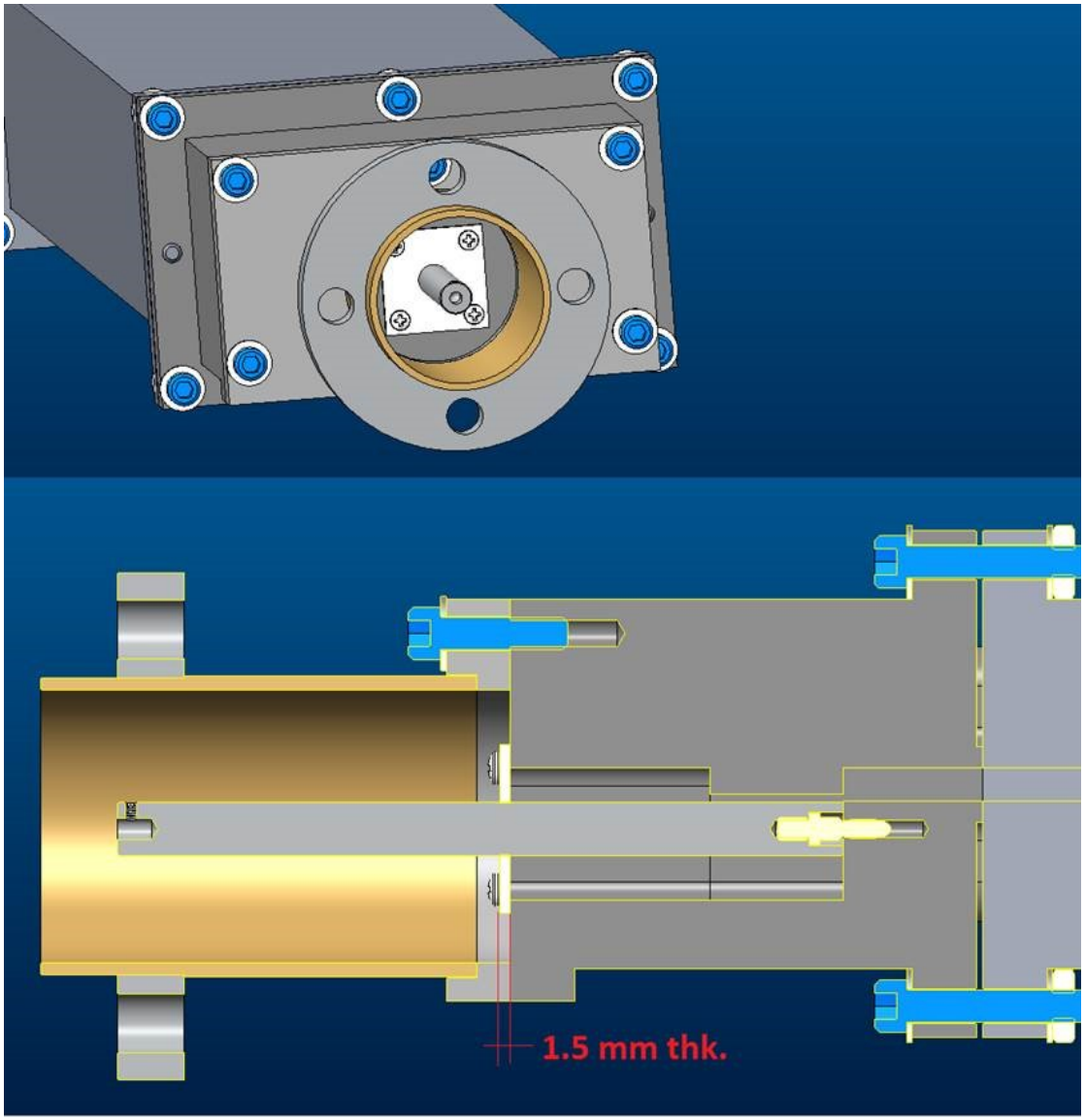

FIGURE 4.13: HOM coupler assembly looking into the cavity side flange (top). Cross sectional view of the antenna assembly attached to the cavity side of the HOM coupler. A 1.5mm thick teflon RF window is used as a support bracket for the antenna (bottom).

Chapter 5

Results

The following chapter outlines the fabrication and performance of the HOM coupler for the BNL3 linac outlined in Chapter 4. The results were compared with previous HOM coupler designs and S_{21} simulations from Section 4.2 for evaluation.

5.1 HOM Coupler Fabrication

One of the preliminary CAD drawings rendered before fabrication of the HOM coupler and the coupler IC can be seen in Figure 5.1. These drawings were checked, approved and released by the Collider Accelerator Department. For initial fabrication the proof of principle HOM coupler was constructed using a full aluminum 6061 body for its mechanical properties, ease of construction and weldability. Much of the fabrication was made possible by machining technique known as wire and sink electric discharge machining (EDM). EDM uses a rapidly recurring current discharging between two electrodes namely, the workpiece electrode and the tool electrode, which are separated by an insulating dielectric fluid to remove material from the workpiece electrode. Once the electrodes are in close proximity, the applied voltage between the two electrodes causes a break down in the dielectric fluid. This causes a spark similar to the breakdown of a capacitor, subsequently removing material from the workpiece. This method allows the machining of intricate channels like the ones seen in Figure 5.2 where conventional milling/grinding would leave behind unwanted edges or ridges and additional machining and tool making is required to remove these features. In addition to intricacy, EDM allows the machining of long channels using a wire electrode with low economic cost and machining time. Thus the half meter long DR WGs seen in Figure 5.3 are easily fabricated with tight tolerances.

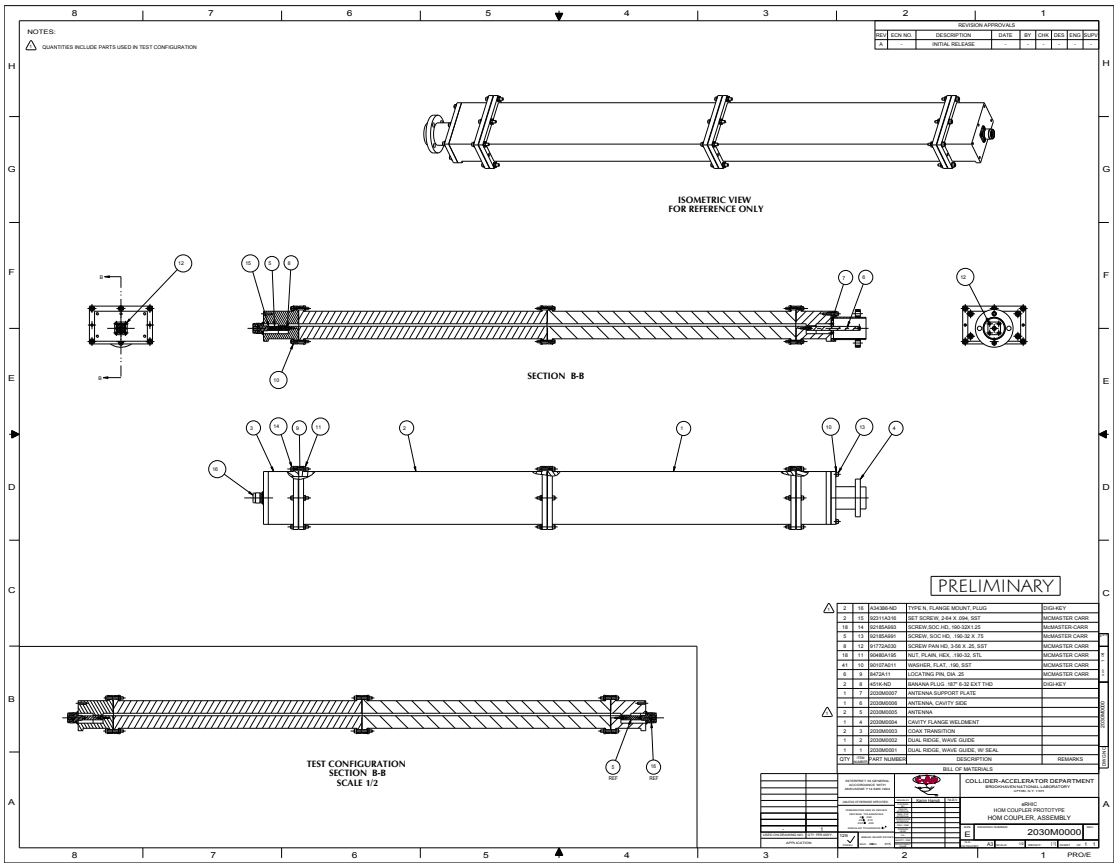

FIGURE 5.1: Preliminary mechanical CAD drawing of the HOM coupler prototype assembly.

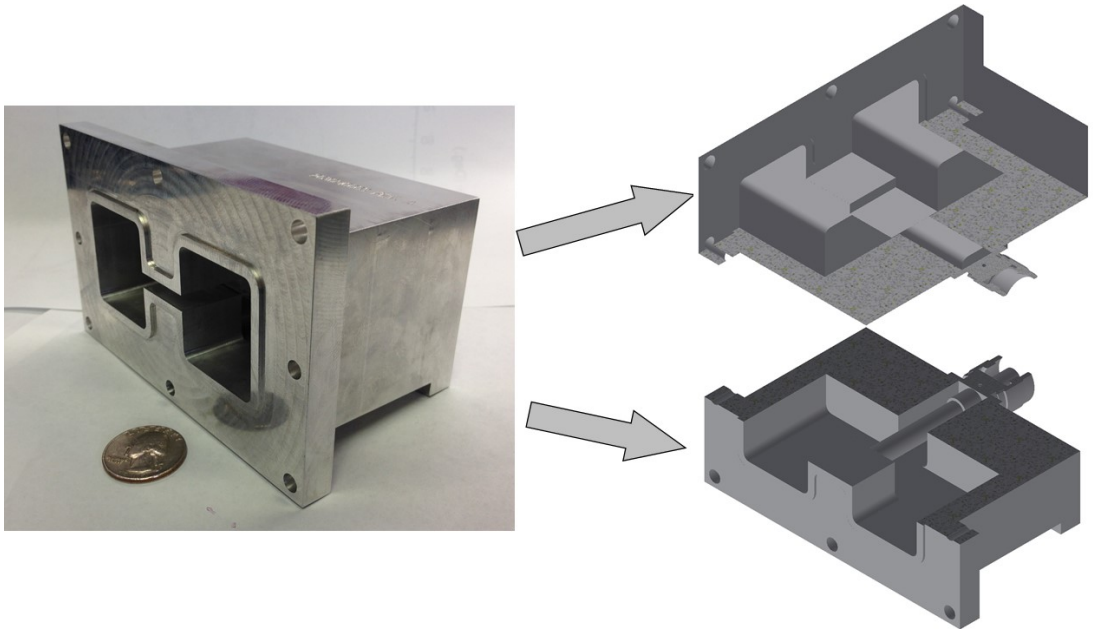

FIGURE 5.2: Photograph of the fabricated HOM coupler IC (left). A cross sectional view inside the mode transitional stage is also shown (right).

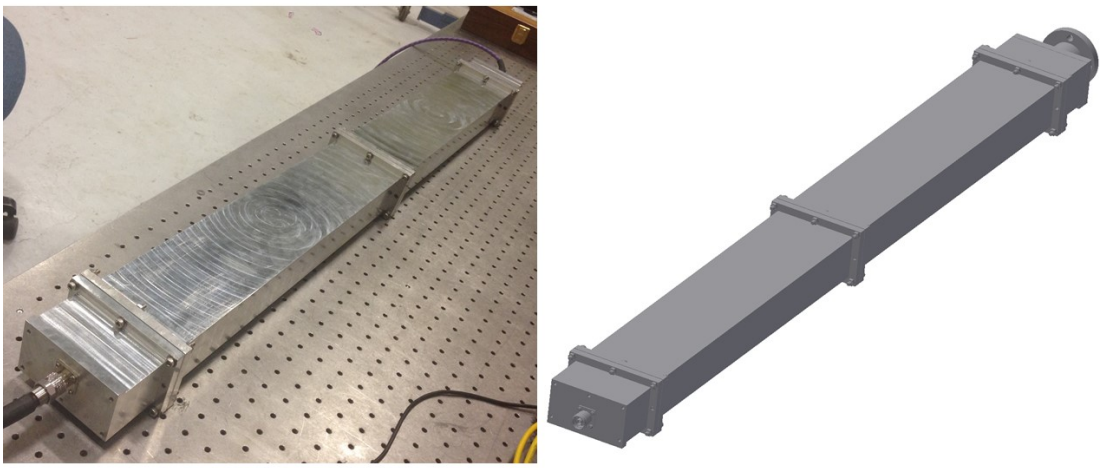

FIGURE 5.3: Photograph of the fabricated coaxial to DR WG HOM coupler (left) and a CAD rendering of the coaxial to DR WG HOM coupler (right)

5.2 Transmission Performance

As mentioned in Section 4.3 the proof of principle HOM coupler will incorporate N-type RF connectors on either sides in addition to the ability of integrating with the BNL3 cavity via a detachable cavity port assembly seen in Figure 4.13 and end tube HOM coupler ports which can be seen in Figure 1.4. The two N-type RF connector ends of the HOM coupler were used to evaluate the S_{21} spectrum and compare this transmission with previous coupler designs and simulations. The measurements were performed by wiring port 1 of the network analyzer to one N-type end of the waveguide and port 2 of the network analyzer to the other end and evaluating various scatter parameters including S_{21} and S_{11} which can be seen in Figure 5.3. After careful calibration to eliminate reflections and impedance from the measurement lines the results from this measurement can be seen in Figure 5.4. The similarity between simulation and measurement shows the precision of the fabrication process and how the simulated model reflects reality. The outcome of the measurements also suggests an excellent rejection of the fundamental mode with -90.65dB transmission using a one meter long DR WG. An average S_{21} scatter parameter of -2.55dB from 825MHz to 4.5GHz suggests an excellent mode conversion from the TEM coaxial modes to the TE propagation mode in the DR WG and back to the TEM coaxial modes as well as impedance matching between all transitions. With these results the prototype coaxial to DR WG design serves as an exceptional candidate for a HOM coupler for the BNL3 linear accelerator.

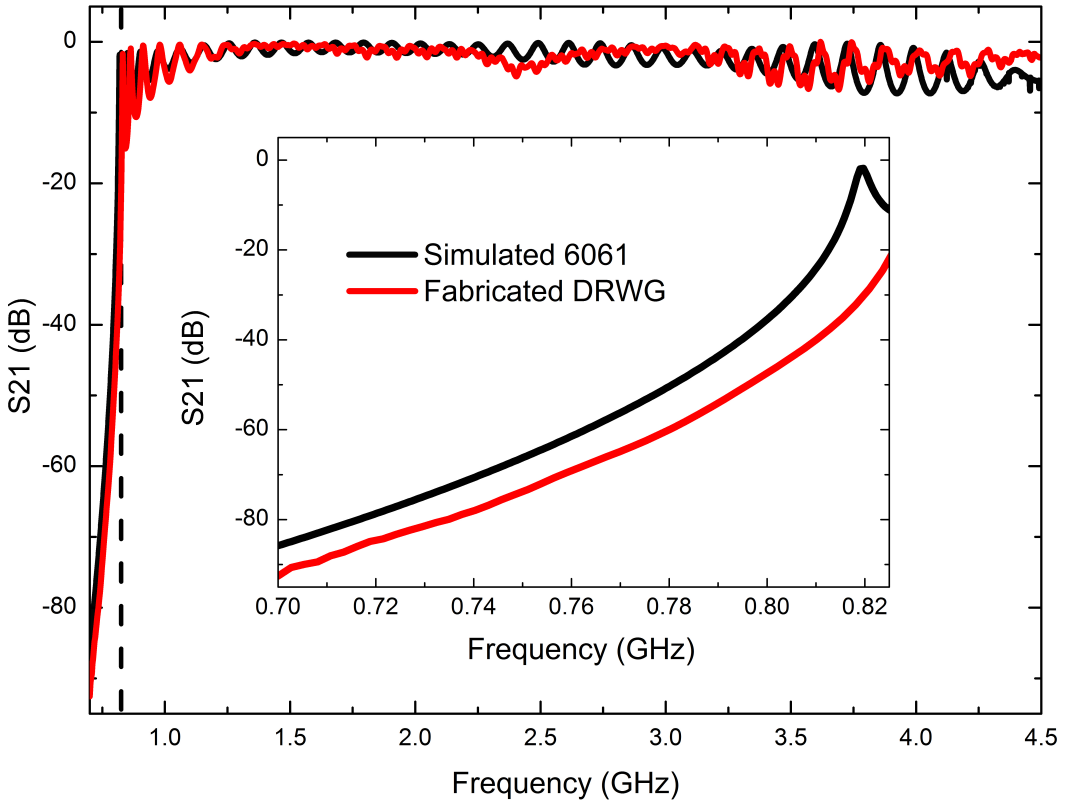

FIGURE 5.4: $S_{21}$of the fabricated DR WG vs. the simulated DR WG with a lossy aluminum 6061 body. Inset shows the transmission S_{21} from the fundamental mode to the first HOM.

5.3 Future Considerations

As discussed in Section 1.3.1, for successful HOM damping approximately 1.25 kW of HOM power must be extracted per HOM coupler per cavity. Therefore power management must be evaluated and executed to meet or exceed this requirement. Among the many possible solutions for RF power management a straight forward approach would be a RF termination load at the end of the waveguide. This RF load will convert the RF power from the HOM coupler into heat which would be dissipated into the surrounding environment. For additional power management ferrite load dampers may line the DR WG. These ferrite dampers must be positioned sufficiently away from the cavity side coupler IC for reasons discussed in Section 1.3.4.

In addition to power handling, the HOM coupler must incorporate a thermal transition from the liquid helium submerged superconducting niobium BNL3 cavity (4K) to outside of the cryostat (300K). The thermal transition analysis may be performed using ANSYS thermal simulation software which is able to correlate the thermal-structural properties with RF performance[23]. The integration of the coaxial to DR WG HOM

coupler to the BNL3 must also be integrated with the cryostat design. With the ability to bend and rotate the coaxial line in addition to slight bending or twisting of the DR WG the cryostat design may be more compact and/or thermal transitions easier to design.

As discussed in Section 1.3.4 a coupling probe or an antenna is responsible to capacitively (or inductively) couple the local field inside the beam tube to the coaxial line of the HOM coupler. With the analysis of HOM characterization performed in Chapter 2 and the coaxial IC design the next step is to create an antenna which couples to potentially dangerous modes and position these antennas appropriately inside and around the BNL3 cavity. A prototype antenna design was fabricated using CST MWS simulations for the HOM coupler designed by Wencan Xu and this design will be integrated and evaluated using the coaxial to DR WG HOM coupler.

Multipacting analysis must also be evaluated to ensure proper operation of the HOM coupler under high power. Multipacting is a resonant process in which a large number of electrons build up spontaneously absorbing rf power resulting in vacuum degradation or discharge and metal sputtering. Fortunately rf structure geometry is used to help prevent the build up of multipacting by establishing electron trajectories towards low energy regions in which the resonance condition is unstable and multipacting is not possible[6]. With the use of wire EDM and abstract geometry deemed fit for antimultipacting will be easily fabricated.

Chapter 6

Conclusion

HOMs pose a realistic threat in the successful operation of accelerator cavities. In this work HOMs were investigated in the next generation ERL cavity the BNL3 and a proof of principal HL-LHC CC through simulations and measurements. Characterization of the HOMs shows excellent correspondence with simulations, suggesting accurate simulated results and a confident measurement technique. The results of the field profile lead to a vantage point to eliminate these problematic excitations and prevent potential BBU in addition to a deeper understanding of discrepancies associated with the construction of these accelerator cavities.

A coaxial to DR WG HOM coupler was designed, simulated, fabricated and integrated to attenuate HOM power while simultaneously rejecting the fundamental mode, ensuring proper cavity performance and excellent beam quality in the BNL3 linear accelerator. The use of a DR WG design promotes compactness, is a natural filter for the fundamental mode and introduces flexibility in terms of fabrication tolerances and actual bending or twisting of the DR WG to allow for additional degrees of freedom in regards to the orientation of the cryostat. A coaxial IC was designed from the waveguide to the cavity to allow additional degrees of freedom when orienting the DR WG with respect to the cavity in turn further reducing the size of the cryomodule. This coaxial to DR WG HOM coupler was compared with previous HOM coupler designs and evaluated using various metrics including RF transmission, real-estate gradient, compactness, ease of fabrication, etc. The promising results show that the HOM coupler is an excellent design for its intended application. Future considerations and solutions were suggested and will be evaluated.

Appendix A

Bead Pulling Improvements

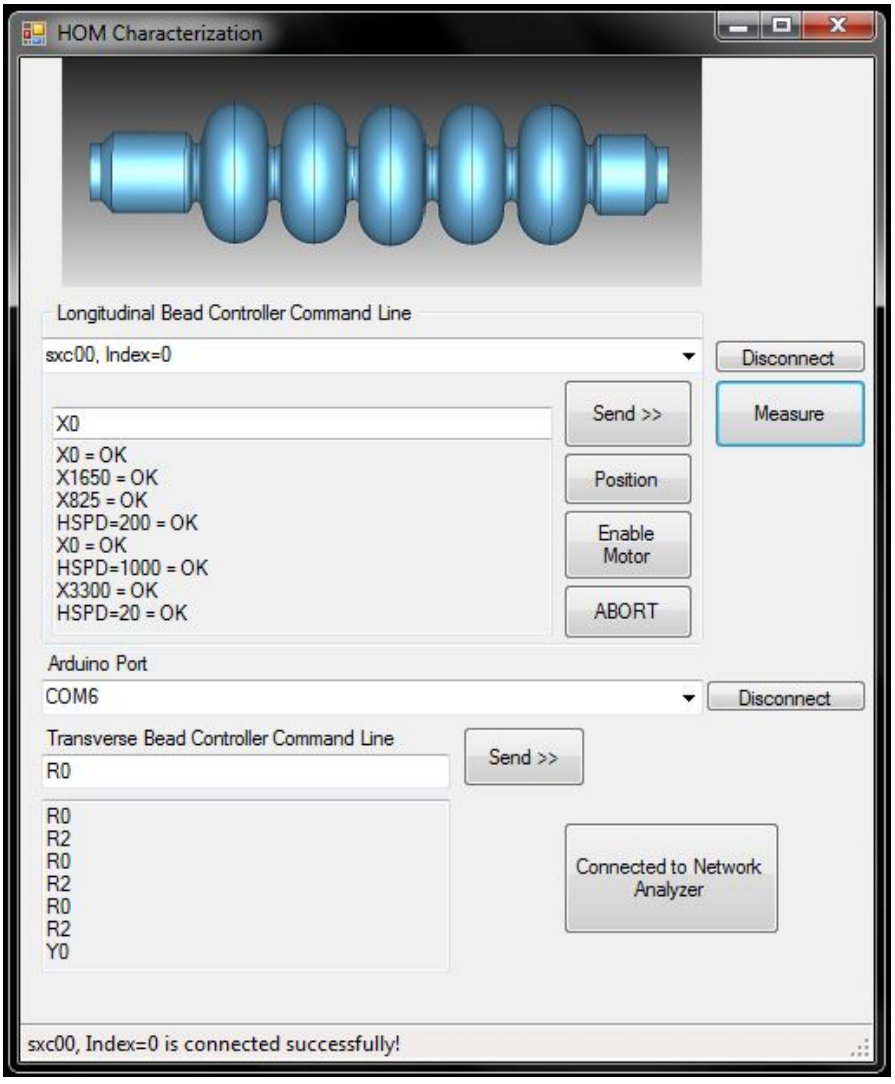

FIGURE A.1: C# program developed for automated control over perturbative bead.

The addition of a computer controlled bead perturbation inside the cavity was a natural step towards understanding and fully characterizing HOMs. The choice of how to control the bead was constrained to a setup which could recycle as much as the original assembly as possible, is easily fabricated, user friendly and relatively inexpensive. With these constraints, the upgrade consisted of an Arduino R3 UNO Microcontroller [24] and Adafruit MotorShield [25] to control the four stepper motors responsible for the x and y translation of the bead. These products are open source, user friendly and each under $30. Microsoft Visual Studio [26] was used to develop code which allowed the integration of the original stepper motor to the upgrade. The code uses serial communication to handshake between both parties of stepper motors and allows us to move the bead in any location with a single program. Microsoft Visual Studio uses a solution file as a structure for organizing project files and the HOM characterization solution file can be acquired upon request from the author. Six hundred and ninty seven lines of code were written to create the resulting C# program in Figure A.1.

The Arduino micro-controller was programmed separately for input/output communication via serial port. Three hundred and one lines of code were written for the Arduino alone, specifically to control the four stepper motors simultaneously through the guidance of the user. A snippet of the code can be seen below,

```
/*********************************************************************************
 * Program description:
 *                   This program is used to control 4 stepper motors via C#
 *                   and serial port communication.
 *                   It uses the Adafruit Motorshield v2 libraries as well as the
 *                   AccelStepper library to define all objects and functions.
 *********************************************************************************/

#include <AccelStepper.h>
#include <Wire.h>
#include <Adafruit_MotorShield.h>
#include "utility/Adafruit_PWMServoDriver.h"

Adafruit_MotorShield AFMSbot(0x61); // Rightmost jumper closed
Adafruit_MotorShield AFMStop(0x60); // Default address, no jumpers

// Connect two steppers with 200 steps per revolution (1.8 degree)
// to the top shield
Adafruit_StepperMotor *myStepper1 = AFMStop.getStepper(200, 1);
Adafruit_StepperMotor *myStepper2 = AFMStop.getStepper(200, 2);

// Connect one stepper with 200 steps per revolution (1.8 degree)
// to the bottom shield
Adafruit_StepperMotor *myStepper3 = AFMSbot.getStepper(200, 1);
Adafruit_StepperMotor *myStepper4 = AFMSbot.getStepper(200, 2);

int LED = 13;   //LED digital input
int Baudrate = 9600;
```

```
float t = 0; //dummy angle
float pi = 3.14159;

float x = 0;
float y = 0;

float spd = 300.0;
float acc = 300.0;

// wrappers for the first motor!
void forwardstep1() {
  myStepper1->onestep(FORWARD, DOUBLE);
}
void backwardstep1() {
  myStepper1->onestep(BACKWARD, DOUBLE);
}
// wrappers for the second motor!
void forwardstep2() {
  myStepper2->onestep(FORWARD, DOUBLE);
}
void backwardstep2() {
  myStepper2->onestep(BACKWARD, DOUBLE);
}
// wrappers for the third motor!
void forwardstep3() {
  myStepper3->onestep(FORWARD, DOUBLE);
}
void backwardstep3() {
  myStepper3->onestep(BACKWARD, DOUBLE);
}
// wrappers for the fourth motor!
void forwardstep4() {
  myStepper4->onestep(FORWARD, DOUBLE);
}
void backwardstep4() {
  myStepper4->onestep(BACKWARD, DOUBLE);
}


// Now we'll wrap the 4 steppers in an AccelStepper object
AccelStepper stepper1(forwardstep1, backwardstep1);
AccelStepper stepper2(forwardstep2, backwardstep2);
AccelStepper stepper3(forwardstep3, backwardstep3);
AccelStepper stepper4(forwardstep4, backwardstep4);
```

All of the command lines operations for the longitudinal bead controller can be found elsewhere [27]. The transverse bead pulling commands are found in Table A.1.

Command	Operation
X###	This command is case insensitive and represents X as in the x-axis. The # represents a number, decimal marker (".") or $\pm$ sign which will be converted to the number of centimeters you wish to move in the x direction for example "X-3.8" or "X4".
Y###	This command is case insensitive and represents Y as in the y-axis. # represents a number, decimal marker (".") or $\pm$ sign which will be converted to the number of centimeters you wish to move in the y direction for example "Y-4.2" or "Y1".
R###	This command is case insensitive and represents R for radius. # represents a number or decimal which will get converted to the radius (in centimeters) for an azimuthal scan for example "R4".
A###	This command is case insensitive and represents A for angle. # represents a number or decimal which will get converted to the angle (in degrees) for a radial scan from the center or initial position five centimeters away and back at the specified angle for example "A340".

TABLE A.1: Relevant transverse bead controller command line controls and description.

Bibliography

[1] A. Deshpande and R. Milner and R. Venugopalan and W. Vogelsang. Study of the Fundamental Structure of Matter with an Electron-Ion Collider. *Annual Review of Nuclear and Particle Science*, 55(1):165–228, 2005. doi: 10.1146/annurev.nucl.54.070103.181218. URL http://www.annualreviews.org/doi/abs/10.1146/annurev.nucl.54.070103.181218.

[2] A. Accardi, J.L. Albacete, M. Anselmino, N. Armesto, E.C. Aschenauer, et al. Electron Ion Collider: The Next QCD Frontier - Understanding the glue that binds us all. 2012. URL http://arxiv.org/abs/1212.1701.

[3] V. Ptitsyn et. al. eRHIC, A Future Electron-Ion Collider at BNL. *Proceedings of the Particle Accelerator Conference, Lucerne, Switzerland*, 2004.

[4] S. M. Gruner et. al. Energy Recovery Linacs as Synchrotron Radiation Sources. *Review of Scientific Instruments*, 73(1402), 2002.

[5] D. Kayran et. al. Status of High Current R&D Energy Recovery Linac at Brookhaven National Laboratory. *Proceedings of the Particle Accelerator Conference , Victora, BC, Canada*, page 455, 2011.

[6] H. Padamsee, J. Knobloch, and T. Hays. *RF Superconductivity for Accelerators*. Wiley series in beam physics and accelerator technology. Wiley-VCH, 2008. ISBN 9783527408429.

[7] D.M. Pozar. *Microwave Engineering, 4th Edition*. Wiley, 2011. ISBN 9781118213636.

[8] W. Xu, I. Ben-Zvi, R. Calaga, H. Hahn, E.C. Johnson, and J. Kewisch. High current cavity design at BNL. *Nuclear Instruments and Methods in Physics Research Section A: Accelerators, Spectrometers, Detectors and Associated Equipment*, 622(1):17 – 20, 2010. ISSN 0168-9002. doi: http://dx.doi.org/10.1016/j.nima.2010.06.245. URL http://www.sciencedirect.com/science/article/pii/S016890021001435X.

[9] S. Deus, P. M. Koch, and L. Sirko. Statistical Properties of the Eigenfrequency Distribution of Three-Dimensional Microwave Cavities. *Phys. Rev. E*, 52:1146–1155, Jul 1995. doi: 10.1103/PhysRevE.52.1146. URL http://link.aps.org/doi/10.1103/PhysRevE.52.1146.

[10] W. Xu, I. Ben-Zvi, S. Belomestnykh, R. Calaga, H. Hahn, E.C. Johnson, and J. Kewisch. High current SRF cavity design for SPL and eRHIC. *Proceedings of the Particle Accelerator Conference , New York, NY*, 2011.

[11] E.C. Johnson. *Higher-Order Modes in the BNL Energy Recovery Linac: Measurement and Waveguide Couple Design"*. Master's thesis, Stony Brook University, 2011.

[12] R. Calaga. *Linear Beam Dynamics and Ampere Class Superconducting RF Cavities at RHIC*. PhD thesis, Stony Brook University, 2006.

[13] CST Microwave Studio, . URL http://www.cst.com/Content/Products/MWS/Overview.aspx.

[14] Agilent E5071C ENA Network Analyzer. URL http://ena.tm.agilent.com/e5071c/manuals/webhelp/eng/.

[15] H. Hahn, I. Ben-Zvi, R. Calaga, L. Hammons, E. C. Johnson, J. Kewisch, V. N. Litvinenko, and Wencan Xu. Higher-Order-Mode Absorbers for Energy Recovery Linac Cryomodules at Brookhaven National Laboratory. *Phys. Rev. ST Accel. Beams*, 13:121002, Dec 2010. doi: 10.1103/PhysRevSTAB.13.121002. URL http://link.aps.org/doi/10.1103/PhysRevSTAB.13.121002.

[16] S. Ramo, J. Whinnery, and T. Van Duzer. *Fields and Waves in Communication Electronics*. John Wiley & Sons Inc., third edition, 1994.

[17] W. Xu, I. Ben-Zvi, S. Belomestnykh, H. Hahn, and E.C. Johnson. New HOM coupler design for high current SRF cavity. *Proceedings of the Particle Accelerator Conference , New York, NY*, 2011.

[18] L.C. Maier and J. C. Slater. Field Strength Measurements in Resonant Cavities. *Journal of Applied Physics*, 23(1):68–77, 1952. ISSN 0021-8979. doi: 10.1063/1.1701980.

[19] H. Hahn, P. Jain, and W. Xu. Study of Split Higher Order Mode Resonances in Superconducting Cavities. *Nuclear Instruments and Methods in Physics Research Section A: Accelerators, Spectrometers, Detectors and Associated Equipment*, 734, Part A(0):44 – 50, 2014. ISSN 0168-9002. doi: http://dx.doi.

org/10.1016/j.nima.2013.06.056. URL http://www.sciencedirect.com/science/article/pii/S0168900213008899.

[20] R. Calaga, E. Ciapala, and E. Jensen. Crab cavities for the lhc luminosity upgrade. *CERN Project Document*, August 2010.

[21] S. B. Cohn. Properties of ridge wave guide. *Proceedings of the IRE*, 35(8):783–788, Aug 1947. ISSN 0096-8390. doi: 10.1109/JRPROC.1947.226277.

[22] Y. Tikhov, I. Sang Song, J. Hwa Won, and J. Phill Kim. Compact broadband transition from double-ridge waveguide to coaxial line. *Electronics Letters*, 39(6): 530–532, March 2003. ISSN 0013-5194. doi: 10.1049/el:20030340.

[23] ANSYS Simulation Software. URL http://www.ansys.com/Products/Simulation+Technology/Structural+Analysis/ANSYS+Mechanical.

[24] Arduino R3 UNO Specifications. URL http://arduino.cc/en/Main/arduinoBoardUno.

[25] Adafruit MotorShield v2 Overview Page. URL http://learn.adafruit.com/adafruit-motor-shield-v2-for-arduino.

[26] Microsoft Visual Studio Overview Page, . URL http://msdn.microsoft.com/en-us/vstudio/aa718325.aspx.

[27] Arcus Technology Single Axis Controller ACE-SXC Manual. URL http://www.arcus-technology.com/support/downloads/category/4-ace.html?download=11%3Aace-sxcmanualrev202.